UNIVERSITY OF BIRMINGHAM
University of Birmingham Research at Birmingham

The motion of a 3D toroidal bubble and its interaction with a free surface near an inclined boundary

Liu, Y; Wang, Qian; Wang, S; Zhang, A. M.

DOI:
10.1063/1.4972771

License:
None: All rights reserved

Document Version
Publisher's PDF, also known as Version of record

Citation for published version (Harvard):
Liu, Y, Wang, Q, Wang, S & Zhang, AM 2016, 'The motion of a 3D toroidal bubble and its interaction with a free surface near an inclined boundary', *Physics of Fluids*, vol. 28, no. 12, 122101. https://doi.org/10.1063/1.4972771

Link to publication on Research at Birmingham portal

Publisher Rights Statement:
Checked for eligibility 22/10/2018

Physics of Fluids 28, 122101 (2016); https://doi.org/10.1063/1.4972771

General rights
Unless a licence is specified above, all rights (including copyright and moral rights) in this document are retained by the authors and/or the copyright holders. The express permission of the copyright holder must be obtained for any use of this material other than for purposes permitted by law.

•Users may freely distribute the URL that is used to identify this publication.
•Users may download and/or print one copy of the publication from the University of Birmingham research portal for the purpose of private study or non-commercial research.
•User may use extracts from the document in line with the concept of 'fair dealing' under the Copyright, Designs and Patents Act 1988 (?)
•Users may not further distribute the material nor use it for the purposes of commercial gain.

Where a licence is displayed above, please note the terms and conditions of the licence govern your use of this document.

When citing, please reference the published version.

Take down policy
While the University of Birmingham exercises care and attention in making items available there are rare occasions when an item has been uploaded in error or has been deemed to be commercially or otherwise sensitive.

If you believe that this is the case for this document, please contact UBIRA@lists.bham.ac.uk providing details and we will remove access to the work immediately and investigate.

Download date: 19. Apr. 2024

The motion of a 3D toroidal bubble and its interaction with a free surface near an inclined boundary

Y. L. Liu, Q. X. Wang, S. P. Wang, and A. M. Zhang

Citation: Physics of Fluids **28**, 122101 (2016); doi: 10.1063/1.4972771
View online: https://doi.org/10.1063/1.4972771
View Table of Contents: http://aip.scitation.org/toc/phf/28/12
Published by the American Institute of Physics

Articles you may be interested in

Numerical analysis of the jet stage of bubble near a solid wall using a front tracking method
Physics of Fluids **29**, 012105 (2017); 10.1063/1.4974073

Modelling for three dimensional coalescence of two bubbles
Physics of Fluids **28**, 062104 (2016); 10.1063/1.4953175

Aerodynamics of two-dimensional flapping wings in tandem configuration
Physics of Fluids **28**, 121901 (2016); 10.1063/1.4971859

Study on the interactions between two identical oscillation bubbles and a free surface in a tank
Physics of Fluids **29**, 052104 (2017); 10.1063/1.4984080

Experimental study on the interaction between bubble and free surface using a high-voltage spark generator
Physics of Fluids **28**, 032109 (2016); 10.1063/1.4944349

Vortex generation and control in a microfluidic chamber with actuations
Physics of Fluids **28**, 122001 (2016); 10.1063/1.4971314

PHYSICS TODAY
WHITEPAPERS

ADVANCED LIGHT CURE ADHESIVES

Take a closer look at what these environmentally friendly adhesive systems can do

READ NOW

PRESENTED BY
MASTERBOND
ADHESIVES | SEALANTS | COATINGS

CrossMark click for updates

PHYSICS OF FLUIDS **28**, 122101 (2016)

The motion of a 3D toroidal bubble and its interaction with a free surface near an inclined boundary

Y. L. Liu,[1] Q. X. Wang,[2,3] S. P. Wang,[1,a)] and A. M. Zhang[1]
[1]*College of Shipbuilding Engineering, Harbin Engineering University, Harbin 150001, China*
[2]*School of Mathematics, University of Birmingham, Edgbaston, Birmingham, United Kingdom*
[3]*School of Naval Architecture, Dalian University of Technology, Dalian 116085, China*

(Received 14 July 2016; accepted 6 December 2016; published online 28 December 2016)

The numerical modelling of 3D toroidal bubble dynamics is a challenging problem due to the complex topological transition of the flow domain, and physical and numerical instabilities, associated with jet penetration through the bubble. In this paper, this phenomenon is modelled using the boundary integral method (BIM) coupled with a vortex ring model. We implement a new impact model consisting of the refined local mesh near the impact location immediately before and after impact, and a surgical cut at a high resolution forming a smooth hole for the transition from a singly connected to doubly connected form. This enables a smooth transition from a singly connected bubble to a toroidal bubble. The potential due to a vortex ring is reduced to the line integral along the vortex ring. A new mesh density control technique is described to update the bubble and free surfaces, which provides a high mesh quality of the surfaces with the mesh density in terms of the curvature distribution of the surface. The pressure distribution in the flow field is calculated by using the Bernoulli equation, where the partial derivative of the velocity potential in time is calculated using the BIM model to avoid numerical instabilities. Experiments are carried out for the interaction of a spark generated bubble with a free surface near a boundary, which is captured by using a high speed camera. Our numerical results agree well with the experimental images, for the bubble and free surface shapes for both before and after jet impact. New results are analyzed for the interaction of a toroidal bubble with a free surface near a vertical boundary and a sloping boundary, at both negative and positive angles to the vertical, without and with buoyancy, respectively. After jet impact, the bubble becomes a bubble ring, whose cross section is much thinner at the distal side from the boundary. It subsequently breaks into a crescent shaped bubble. The free surface displays singular features at its intersection with an inclined boundary. *Published by AIP Publishing.* [http://dx.doi.org/10.1063/1.4972771]

I. INTRODUCTION

A bubble is generated after the shock wave when a charge explodes underwater. It will cause severe damage to its nearby structures. A high-speed liquid jet often forms during nonspherical collapse of a bubble, which subsequently impacts on the opposite bubble wall, and penetrates through the bubble, forming a toroidal bubble. High-speed bubble jets impinging on a rigid boundary are believed to be associated with cavitation damage to pumps, turbines, and propellers (Young, 1989; Brennen, 1995; Magnaudet and Eames, 2000; Lauterborn and Vogel, 2013; Hsiao *et al.*, 2014; Huang *et al.*, 2013; and Ji *et al.*, 2014), as well as a part of the damage associated with underwater explosions (Cole, 1948; Chahine and Bovis, 1980; Klaseboer *et al.*, 2005a; Jayaprakash *et al.*, 2011; and Jayaprakash *et al.*, 2012). This mechanism is also believed responsible for ultrasonic cleaning

a)Author to whom correspondence should be addressed. Electronic mail: wangshiping@hrbeu.edu.cn.

(Song *et al.*, 2004; Ohl *et al.*, 2006; and Lauterborn and Kurz, 2010). In sonochemistry, bubble jetting due to ultrasound may accelerate chemical reactions (Blake *et al.*, 1999; Fernandez Rivas *et al.*, 2013; and Zhang *et al.*, 2016a). Toroidal bubble dynamics are essential for studying these applications.

Bubble dynamics before jet impact have been extensively studied theoretically, experimentally, and numerically (Rayleigh, 1917; Plesset and Prosperetti, 1977; Blake and Gibson, 1987; Leighton, 1994; Brennen, 1995; Feng and Leal, 1997; Lauterborn *et al.*, 1999; Lauterborn and Kurz, 2010; Zhang and Liu, 2015; and Zhang *et al.*, 2016b). However, the jet impact and subsequent toroidal bubble dynamics have been much less investigated in the literature.

The liquid domain becomes doubly connected after jet impact, which results in a non-unique solution problem for a potential flow model. The doubly connected domain can be made singly connected by, for example, using a branch cut by Best (1993) or a vortex sheet by Zhang *et al.* (1993) and Zhang and Duncan (1994). Wang *et al.* (1996) and Wang *et al.* (2005) developed a vortex ring model, to model the topological transition of a bubble and the subsequent toroidal bubble dynamics. Bonometti and Magnaudet (2006) and Bonometti and Magnaudet (2007) simulated the rising, deforming, and topological transition of a two-dimensional bubble in a viscous fluid, using an advanced interface-capturing method based on the Navier-Stokes equations. Hsiao *et al.* (2014) developed a hybrid approach, using the boundary integral method (BIM) to simulate a bubble collapsing near an elastic boundary and the compressible finite difference method to simulate the subsequent jet impact and toroidal bubble dynamics. Han *et al.* (2015) simulated laser induced bubble pairs using the OpenFOAM based on the volume-of-fluid (VOF) method, and their results agreed well with experiments for the toroidal phase.

Very few simulations in the literature are for three dimensional (3D) toroidal bubbles (Zhang *et al.*, 2001; Wang *et al.*, 2003; Klaseboer *et al.*, 2005a; and Zhang and Liu, 2015) due to the challenges associated with the complex topological change of the flow domain, and the physical and numerical instabilities, associated with jet impact, jet penetration through the bubble, and bubble rebound. In this paper, 3D toroidal bubbles are modeled using the BIM model, coupled with a new impact model and a vortex ring model. After jet impact, numerically a "hole" must be made by a surgical cut procedure to allow the liquid to penetrate through the bubble. To overcome the shortcomings of the numerical instabilities after the surgical cut procedure at the first ring around the impact node (Zhang *et al.*, 2001), the second ring cut is performed in this paper. A local mesh refinement is executed near the impact location to reduce the numerical errors. With this procedure, a high resolution and smooth hole is generated, enabling a smooth transition from a singly connected bubble to a toroidal bubble. The potential due to a vortex ring was calculated using a solid angle formula, which leads to unacceptable errors for points close to the vortex surface because of the poor quality of the tetrahedron (Zhang *et al.*, 2001 and Curtiss *et al.*, 2013). In this paper, the potential of a 3D vortex ring is calculated by integrating the velocity associated from infinity to the field point to avoid the numerical inaccuracy using a solid angle formula (Wang *et al.*, 1996 and Zhang and Liu, 2015). The criterion on the choice of the integral path is provided.

Another challenge associated with the phenomenon is to calculate the pressure distribution generated by bubble dynamics, which are essential to analyze bubble dynamics and to estimate its damage potential. There are very few calculations for the pressure field associated with axisymmetric toroidal bubbles (Pearson *et al.*, 2004a; Hsiao *et al.*, 2013; and Han *et al.*, 2015). We consider 3D cases using the potential flow model, where the pressure is calculated using the Bernoulli equation in the potential flow theory. The difficulty lies on the calculation of $\partial\varphi/\partial t$, a term in the Bernoulli equation, where φ is the velocity potential. To calculate $\partial\varphi/\partial t$ using the finite difference method often results in unaccepted errors because the time steps used for simulating violent collapsing bubbles are very small. We will calculate $\partial\varphi/\partial t$ using the BIM model (Tanizawa, 1995 and Wu, 1998).

In this paper, we consider a toroidal bubble and its interaction with a free surface near an inclined boundary, which is associated with underwater explosion bubble dynamics near a shipboard or a dam. To cope with the topological difficulties of the moving mesh along the inclined boundary, the image method is introduced. To validate the numerical model, experiments are carried out for the interaction of a spark generated bubble with a free surface near a boundary in a water tank, which is captured by

using a high speed camera. Our numerical results agree well with the experimental images, for the bubble surface and free surface shapes, both before and after jet impact.

With the validated model, we simulate the interaction of a toroidal bubble and a free surface near a rigid boundary, which are associated with applications for underwater explosions (Cole, 1948; Chahine and Perdue, 1990; Klaseboer *et al.*, 2005a; Hung and Hwangfu, 2010; and Wang, 2013) and seismic airgun operations (Caldwell, 2002; Cox *et al.*, 2004; Madsen *et al.*, 2006; Chen *et al.*, 2008; and Barker and Landrø, 2014). The bubble and free surface interaction near a vertical boundary was modelled by Zhang *et al.* (1998), Wang *et al.* (2003), Wang (2004), and Liu *et al.* (2013), using the BIM model. We carry out the following three developments to these works: (i) the modelling of toroidal bubbles, (ii) the calculation of the pressure and velocity distributions of the flow field, and (iii) the analysis of the effects of the inclined boundary. We model the interaction near an inclined boundary, since a sloping boundary, at negative and positive angles to the vertical may represent a vessel hull and a dam, respectively. Our calculations show that the free surface displays singular features at its intersection with the boundary.

II. PHYSICAL AND MATHEMATICAL MODEL

Consider the interaction of a gas bubble with a free surface near an inclined rigid boundary, as shown in Figure 1. A Cartesian coordinate system $Oxyz$ is set, with the origin at the centre of the initial spherical bubble, and the z-axis in the direction opposite gravity. The depth of the bubble centre at inception is denoted as d_1, and its standoff distance from the rigid boundary is d_2. The inclined angle of the boundary α is measured from the z-axis, being positive counter clockwise. As $\alpha < 0$, it is termed as a flaring boundary, which may represent bubble dynamics near a vessel hull. As $\alpha > 0$, it is termed as a fall in the boundary, which may represent bubble dynamics near a dam.

The flow is assumed to be incompressible, inviscid, and irrotational. The fluid velocity $\boldsymbol{v}$ thus has a potential φ, $\boldsymbol{v} = \nabla\varphi$ satisfying Laplace's equation,

$$\nabla^2\varphi = 0. \tag{2.1a}$$

The kinematic boundary conditions on the boundary S_W, bubble surface S_B, free surface S_F, and at infinity are as follows:

$$\frac{\partial\varphi}{\partial n} = 0 \text{ on } S_W, \tag{2.1b}$$

$$\frac{D\boldsymbol{r}}{Dt} = \nabla\varphi \text{ on } S_B \text{ and } S_F, \tag{2.1c}$$

$$\nabla\varphi \to 0 \text{ as } r \to \infty, \tag{2.1d}$$

where $\boldsymbol{r}$ is the position vector of the boundary, $\boldsymbol{n}$ is the normal on the boundary surface D/Dt denotes the material derivative, and $r = |\boldsymbol{r}|$ is the length of a vector $\boldsymbol{r}$. (2.1b) is the impermeable

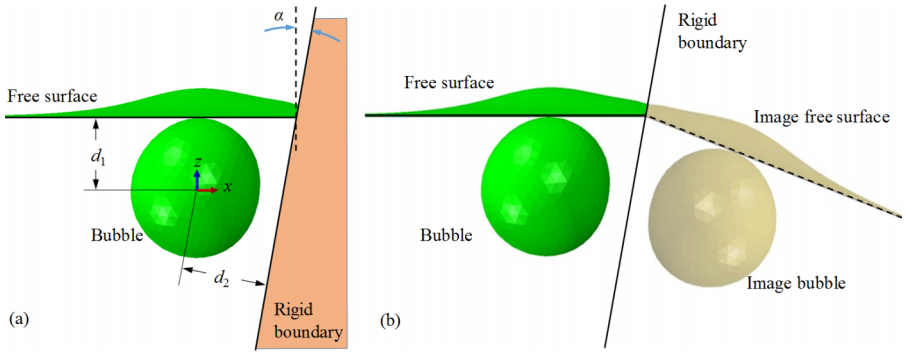

FIG. 1. (a) Configuration and coordinate system for bubble dynamics near a free surface and an inclined rigid plane boundary. The inclined boundary is with an angle α with the z-axis, the depth of the bubble centre at inception is denoted as d_1, and its standoff distance from the rigid boundary is d_2. (b) Illustration of the method of image.

boundary condition on the rigid boundary, and (2.1c) requires a node on the bubble or free surfaces to remain on them.

We assume that the pressure inside the bubble is uniform, since the density of gases is usually three orders of magnitude smaller than that of liquids. We assume also that the expansion and contraction of the bubble gases occur adiabatically. The pressure of the bubble gas p_B is thus given by

$$p_B = p_0\left(\frac{V_0}{V}\right)^{\kappa}, \tag{2.1e}$$

where p_0 is the initial gas pressure inside the bubble, V and V_0 are the instantaneous and initial bubble volumes, respectively, and κ is the polytropic coefficient (Best and Kucera, 1992). We take $\kappa = 1.25$ in this paper. Additionally, heat and mass transfer across the bubble surface can be included (cf. Szeri *et al.*, 2003) but are neglected here.

The dynamic boundary conditions on the bubble surface S_B and free surface S_F require that the pressure is continuous across the two surfaces, which can be written as follows by using the Bernoulli equation:

$$\frac{D\varphi}{Dt} = \frac{1}{2}|\nabla\varphi|^2 - gz \text{ on } S_F, \tag{2.1f}$$

$$\frac{D\varphi}{Dt} = \frac{p_\infty}{\rho} + \frac{1}{2}|\nabla\varphi|^2 - g\,(z - d_1) - \frac{p_B}{\rho} \text{ on } S_B, \tag{2.2}$$

where g is the acceleration of gravity, p_∞ is the hydrostatic pressure at the origin, and ρ is the fluid density. The Weber number $W_e = R_m p_\infty/\sigma$, where $\sigma = 0.0728$ N/m is the surface tension coefficient, R_m is the equivalent radius at the bubble's maximum volume, and Reynolds number $R_e = \left(R_m\sqrt{p_\infty/\rho}\right)/\upsilon$, where $\upsilon = 1.0037\times10^{-6}$ m^2/s is the kinematic coefficient of viscosity at 20 °C. For example, when a 200 kg TNT explodes at 7.6 m beneath the free surface, the maximum bubble radius generated is 7.6 m with the corresponding Weber number equaling to 1.1×10^7 and Rayleigh number equaling to 10^8 which indicates both the surface tension and the viscous effects are ignorable. It has been concluded that these two effects are considered only for tiny bubbles (Wang and Blake, 2010; Wang and Blake, 2011; and Wang and Manmi, 2014). The surface tension and viscous effects are neglected here.

The potential φ may be represented as an integral over the bubble surface S_B and free surface S_F as follows, using Green's second identity:

$$c\,(\boldsymbol{r},t)\,\varphi\,(\boldsymbol{r},t) = \int\limits_{S_B+S_F}\left(\frac{\partial\varphi\,(\boldsymbol{q},t)}{\partial n}G(\boldsymbol{r},\boldsymbol{q}) - \varphi(\boldsymbol{q},t)\frac{\partial G(\boldsymbol{r},\boldsymbol{q})}{\partial n}\right)dS\,(\boldsymbol{q})\,, \tag{2.3}$$

where $\boldsymbol{q}$ is the source point varying as an integration variable on the boundary and $c(\boldsymbol{r},t)$ is the solid angle. To satisfy the impermeable boundary condition on the rigid boundary, the Green function is given as follows using the method of image:

$$G(\boldsymbol{r},\boldsymbol{q}) = \frac{1}{|\boldsymbol{r}-\boldsymbol{q}|} + \frac{1}{|\boldsymbol{r}-\boldsymbol{q}'|}, \tag{2.4}$$

where $\boldsymbol{q}'$ is the image of $\boldsymbol{q}$ reflected to the rigid boundary, and the boundary conditions on the boundary and at infinity ((2.1b) and (2.1d)) are satisfied automatically.

We choose the hydrostatic pressure p_∞ as the reference pressure, and the maximum equivalent radius of the bubble $R_m = \left(\frac{3}{4\pi}V_m\right)^{1/3}$ as the reference length, where V_m is the maximum bubble volume. The phenomenon is largely affected by the following two dimensionless depth γ_f and dimensionless standoff distance from the boundary γ_w,

$$\gamma_f = {}^{d_1}/_{R_m}, \quad \gamma_w = {}^{d_2}/_{R_m}, \tag{2.5}$$

where d_1 and d_2 are the distances of the bubble centre at bubble inception from the free surface and rigid boundary, respectively.

The dimensionless dynamical boundary conditions ((2.1e) and (2.1f)) become

$$\frac{D\varphi_*}{Dt_*} = \frac{1}{2}|\nabla_*\varphi_*|^2 - \delta^2 z_* \text{ on } S_F, \tag{2.5a}$$

$$\frac{D\varphi_*}{Dt_*} = 1 + \frac{1}{2}|\nabla_*\varphi_*|^2 - \delta^2\left(z_* - \gamma_f\right) - \varepsilon\left(\frac{V_{*0}}{V_*}\right)^{\kappa} \text{ on } S_B, \tag{2.5b}$$

where the dimensionless quantities are denoted by a subscript *, $\delta = \sqrt{\rho g R_m/p_\infty}$ is the buoyancy parameter, and $\varepsilon = p_0/p_\infty$ is the dimensionless initial bubble pressure, which is set as $\varepsilon = 100$ for the calculations in this paper unless stated otherwise. The time is nondimensionalized by $R_m\sqrt{\rho/p_\infty}$.

The bubble is assumed to begin its existence at $t_* = 0$ as a high pressure spherical bubble with radius R_{*0} and zero radial velocity, where the initial radius R_{*0} is solved by the reverse time integration of the Rayleigh-Plesset equation (Best and Blake, 1994 and Wang, 2013). The quiescent initial state is given, i.e., $\varphi = 0$ throughout the entire fluid domain.

III. MODELING FOR 3D TOROIDAL BUBBLES

A. Impact modelling

Jet impact often occurs at a single point, since the curvature of the jet front is usually larger than that of the opposite bubble surface. We restrict it to this idealized model. In reality, jet impact may be more complex: jet impact may occur at a small area, when the curvatures of the jet front and the opposite bubble surface at the impact location are approximately equal, or at a ring when the curvature of the jet front is smaller.

We first identify two impact nodes, N and S (one on the jet front and the other on the opposite bubble boundary, respectively). The two nodes are selected when the distance between them is within the average element size at the impact nodes. To avoid having "false" impact node S from the neighbours of node N (this would mean that the jet impacts on itself), the angle between the normal vectors at the two nodes is set larger than $3\pi/4$.

Once the impact nodes N and S are identified, numerically a "hole" must be made by a surgical cut procedure to allow the fluid to go through (Klaseboer *et al.*, 2005a). At each impact node, the first and second rings of neighbouring nodes are shown in Figure 2(a), and the top view of the toroidal bubble after the surgical cut at the second ring is shown in Figure 2(b). Zhang *et al.* (2001) performed the cut at the location of the first ring to make the hole. Because the first ring consists of only 5 to 7 nodes, the hole of the bubble torus is like a prism with about 5 to 7 sides, each of them consisting of two plane triangles. The hole/eye of the bubble torus is thus not smooth, and this can cause numerical instabilities subsequently.

We perform the surgical cut at the second ring, consisting of 10 to 14 nodes, and thus a relatively smooth hole/eye of the bubble torus can be formulated. This is essential for avoiding numerical instability during the toroidal phase. However, a larger portion of the bubble volume is cut away in this approach as compared to the surgical cut at the first ring. To reduce the associated numerical errors with the new approach, the local mesh near the impact location is refined before the surgical cut. The details of the mesh control techniques are to be described in Sec. III D. The meshes of the bubble surface before and after mesh refinement are shown in Figures 2(c) and 2(d), respectively. The mesh refinement is carried out using the density potential method (Zhang and Liu, 2015). Before the mesh refinement, the line segments between neighbouring nodes on the second ring on the jet front are much shorter than those on the second ring on the opposite bubble wall. With the same mesh density prescribed in the density potential method at the two areas, the segment lengths on both the second rings are comparable after the mesh refinement. This further helps in improving the smoothness and mesh quality of the eye. The starting geometry and mesh of the toroidal bubble, obtained by using the new surgical cut, are shown in Figure 2(b) for the top view and Fig. 2(e) for the side view, respectively, where the eye of the toroidal bubble is much smoother than that in Zhang *et al.* (2001).

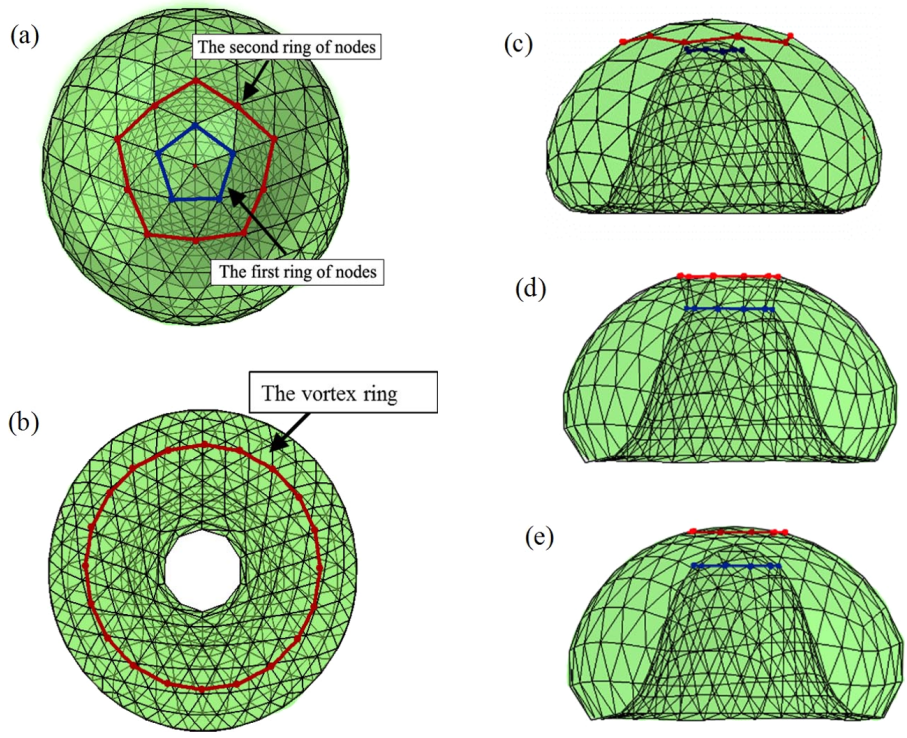

FIG. 2. Illustration of the impact model: (a) Top view of the bubble before jet impact with the first and second rings of neighbour nodes to an impact node, (b) top view of the toroidal bubble by the improved surgical cut along the second ring, (c) side view of the bubble before impact with the mesh before mesh refinement, (d) side view of the bubble before impact after mesh refinement, and (e) the side view.

To perform the surgical cut automatically, a local coordinate O-XYZ is introduced with its origin at the node N and its Z-axis passing the node S. We reorder the neighbour nodes on the two rings according to their azimuth angles, as $N_1N_2 \ldots N_{\mathrm{m}}$ associated with the node N and as $S_1S_2 \ldots S_{\mathrm{m}}$ associated with the node S, respectively. When the node numbers of the two sets are not equal, additional nodes will be added to the ring with the less nodes to make them even. Triangles are then connected among the neighboring nodes. Each of the triangles consists of two neighboring nodes on one of the two rings and another node from the other ring. It is not necessary to add additional nodes to make the nodes on the two rings identical as performed by Zhang *et al.* (2001).

B. 3D vortex ring modelling

Jet impact transforms a simply connected bubble into a toroidal bubble, generating a circulation to the flow around the bubble ring. In the vortex ring model, a vortex ring is placed inside the toroidal bubble after jet impact, in such a way that the hole of the bubble is going through the ring. The strength Γ of the vortex ring is equal to the jump of the potential φ across the contact points N and S at the time of impact to account for the circulation generated by jet impact, as illustrated in Figure 3. Thus,

$$\Gamma = \varphi_N - \varphi_S, \tag{3.1}$$

where φ_N and φ_S are potentials at the impact points (Wang *et al.*, 2005). The circulation Γ is invariant in time as the potential satisfies Laplace's equation.

In theory, the precise location of the vortex ring is immaterial, as long as it lies completely within the toroidal bubble. However, if the distance between the vortex ring and the bubble surface is comparable to the element size, the numerical errors associated with the calculation of the potential of the vortex ring may result in numerical instabilities. As such, the vortex ring should not be

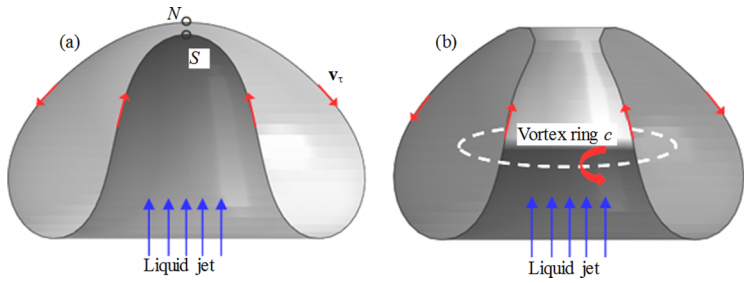

FIG. 3. Illustration of the numerical transition of the bubble shape and the vortex ring model: (a) immediately before and (b) immediately after jet impact, when a vortex ring placed inside the toroidal bubble.

too close to the bubble surface. We place each node of the vortex ring at the farthest point from the associated cross section of the bubble ring in the azimuth plane (Zhang and Liu, 2015).

With the vortex ring placed in the bubble ring, the potential φ is now decomposed as follows:

$$\varphi(\boldsymbol{r},t) = \varphi_{vr}(\boldsymbol{r}) + \phi(\boldsymbol{r},t), \tag{3.2}$$

where φ_{vr} is the potential of the vortex-ring, $\boldsymbol{r} = (x, y, z)$. With the potential jump being accounted for the vortex ring using (3.2), the remnant potential ϕ is continuous in the flow field.

For convenience, we assume that the potential of the vortex ring satisfies the impermeable boundary condition and vanishes at infinity, i.e.,

$$\frac{\partial \varphi_{vr}}{\partial n} = 0 \text{ on } S_W, \tag{3.3a}$$

$$\varphi_{vr}(\boldsymbol{r}) = 0 \text{ as } \boldsymbol{r} \to \infty. \tag{3.3b}$$

After the potential for a vortex ring in an unbounded flow field, φ_{vr} satisfying condition (3.3a) can be obtained by using the method of image.

Substituting (3.2) and (3.3) into (2.1), one can obtain the boundary value problem for the remnant potential ϕ as follows:

$$\nabla^2\phi = 0, \tag{3.4a}$$

$$\frac{\partial \phi}{\partial n} = 0 \text{ on } S_W, \tag{3.4b}$$

$$\frac{D\boldsymbol{r}}{Dt} = \boldsymbol{v}_{vr} + \nabla\phi \text{ on } S_B \text{ and } S_F, \tag{3.4c}$$

$$\nabla\phi \to 0 \text{ as } r \to \infty, \tag{3.4d}$$

$$\frac{D\phi}{Dt} = \nabla\phi \cdot (\boldsymbol{v}_{vr} + \nabla\varphi) - \frac{1}{2}|\boldsymbol{v}_{vr} + \nabla\varphi|^2 - gz \text{ on } S_F, \tag{3.4e}$$

$$\frac{D\phi}{Dt} = 1 + \nabla\phi \cdot (\boldsymbol{v}_{vr} + \nabla\varphi) - \frac{1}{2}|\boldsymbol{v}_{vr} + \nabla\varphi|^2 - g(z-d) - \frac{p_B - p_\infty}{\rho} \text{ on } S_B. \tag{3.4f}$$

The above governing equations for the remnant potential ϕ are in the same format as Equations (2.1) for the potential φ for the pre-toroidal phase. ϕ thus can be solved using the BIM approach developed for φ.

C. Calculation of potential due to a vortex ring

Zhang *et al.* (2001) calculated the potential due to a vortex ring using the solid angle formula referred in Milne-Thompson (1968),

$$\varphi_{vr} = \frac{\Gamma}{4\pi}\int_{S_c} \frac{\partial G(\boldsymbol{r},\boldsymbol{q})}{\partial n} dS(\boldsymbol{q}), \tag{3.5}$$

where S_c is any surface enclosed by the vortex ring. This integral is associated with discontinuity when the field points $\boldsymbol{r}$ are on any plane that is tangent to the vortex ring c, and so this approach leads to unacceptable errors at these points (Curtiss *et al.*, 2013).

The velocity field $\boldsymbol{v}_{vr}$ induced by a vortex ring is given by the Biot-Savart law,

$$\boldsymbol{v}_{vr}(\boldsymbol{r}) = \nabla\varphi_{vr}(\boldsymbol{r}) = \frac{\Gamma}{4\pi}\oint_{\boldsymbol{c}} \frac{\boldsymbol{\tau}\times\boldsymbol{R}}{R^3}dl, \quad \boldsymbol{R} = \boldsymbol{r} - \mathbf{q}, \tag{3.6}$$

where the line integral is along the vortex ring c, $\boldsymbol{q}$ is the moving point of the integration on c, and $\boldsymbol{\tau}$ is the unit tangential vector of curve c at point $\boldsymbol{q}$. The potential due to the vortex ring can be calculated by performing the line integral of the velocity (3.6) from infinity to the point considered along an arbitrary path.

Assume that the jet is along the z-axis and this can always be satisfied with a coordinate transform. The potential at a field point $\boldsymbol{r} = (x, y, z)$ due the vortex ring can be calculated by integrating the velocity of (3.5) along a straight line parallel to the z-axis from (x, y, ∞) or $(x, y, -\infty)$ to (x, y, z),

$$\varphi^{\pm}_{vr}(\boldsymbol{r}) = -\int_{\pm\infty}^{z} \boldsymbol{v}_{vr}(\boldsymbol{r})\cdot\boldsymbol{k}dz = -\frac{\Gamma}{4\pi}\int_{\pm\infty}^{z}\oint_{\boldsymbol{c}} \frac{\boldsymbol{\tau}\times\boldsymbol{R}}{R^3}dl\cdot\boldsymbol{k}\,dz = -\frac{\Gamma}{4\pi}\oint_{\boldsymbol{c}}\int_{\pm\infty}^{z} \frac{\boldsymbol{\tau}\times\boldsymbol{R}}{R^3}\cdot\boldsymbol{k}dldz, \tag{3.7}$$

where $\boldsymbol{k}$ is the unit coordinate vector of the z-axis. The order of the integrations was changed because the curve c for the line integral does not depend on z. It is assumed in (3.7) that $\varphi^{\pm}_{vr}(\boldsymbol{r}) = 0$ as $\boldsymbol{r}\to\infty$.

Only the z-component of $\boldsymbol{R}$ in the integrant of (3.7) depends on z. It is easy to verify that $\boldsymbol{\tau}\times\boldsymbol{R}\cdot\mathbf{k}dl$ does not depend on z, since

$$\boldsymbol{\tau}\times\boldsymbol{R}\cdot\boldsymbol{k}dl = \boldsymbol{\tau}\cdot\boldsymbol{R}\times\boldsymbol{k}dl = \boldsymbol{\tau}\cdot\left(-R_x\boldsymbol{j} + R_y\boldsymbol{i}\right)dl, \tag{3.8}$$

where R_x and R_y are the x- and y-components of $\boldsymbol{R}$, respectively, and $\boldsymbol{i}$ and $\boldsymbol{j}$ are the unit coordinate vectors of the x- and y-axes, respectively. Therefore the inner integral of (3.7) can be written as

$$\int_{\pm\infty}^{z} \frac{\boldsymbol{\tau}\times\boldsymbol{R}}{R^3}dl\cdot\boldsymbol{k}dz = \boldsymbol{\tau}\times\boldsymbol{R}\cdot\boldsymbol{k}\int_{\pm\infty}^{z}\frac{1}{R^3}dzdl. \tag{3.9}$$

The integral on the right hand side of (3.9) can be integrated analytically,

$$\int_{\pm\infty}^{z}\frac{1}{R^3}dz = \int_{\pm\infty}^{z}\frac{dz}{\left(R_r^2 + (z - c_z(\theta))\right)^{3/2}} = \int_{\pm\infty}^{z-q_z}\frac{d\eta}{\left(R_r^2+\eta^2\right)^{3/2}} = \left.\frac{\eta}{R_r^2\sqrt{R_r^2+\eta^2}}\right|_{\pm\infty}^{z-q_z} = \frac{1}{R_r^2}\left(\frac{R_z}{R}\mp 1\right), \tag{3.10}$$

where R_z and R_r are the z-component and radial component of $\boldsymbol{R}$, respectively, and q_z is the z-component of $\boldsymbol{q}$.

Substituting (3.9) and (3.10) into (3.7) yields

$$\varphi^{\pm}_{vr}(\boldsymbol{r}) = \frac{\Gamma}{4\pi}\oint_{\boldsymbol{c}}\frac{1}{R_r^2}\left(\frac{R_z}{R}\mp 1\right)\boldsymbol{k}\cdot\boldsymbol{R}\times\boldsymbol{\tau}dl. \tag{3.11}$$

More specifically the potential of the vortex ring obtained by the integration along the straight line from (x, y, ∞) to (x, y, z) is

$$\varphi^{+}_{vr}(\boldsymbol{r}) = \frac{\Gamma}{4\pi}\oint_{\boldsymbol{c}}\frac{1}{R_r^2}\left(\frac{R_z}{R} - 1\right)\boldsymbol{k}\cdot\boldsymbol{R}\times\boldsymbol{\tau}dl, \tag{3.12}$$

and the potential integrated along the straight line from $(x, y, -\infty)$ to (x, y, z) is

$$\varphi^{-}_{vr}(\boldsymbol{r}) = \frac{\Gamma}{4\pi}\oint_{\boldsymbol{c}}\frac{1}{R_r^2}\left(\frac{R_z}{R} + 1\right)\boldsymbol{k}\cdot\boldsymbol{R}\times\boldsymbol{\tau}dl. \tag{3.13}$$

The potential due to a vortex ring is reduced as the integration along the vortex ring, which is subsequently calculated numerically.

It can be proven that

$$\varphi_{vr}^{+}(\boldsymbol{r}) - \varphi_{vr}^{-}(\boldsymbol{r}) = \begin{cases} 0 \text{ as } (x,y,0) \text{ is outside of } c_z, \\ \Gamma \text{ as } (x,y,0) \text{ is inside of } c_z, \end{cases} \tag{3.14}$$

where c_z is the enclosed curve projecting the vortex ring c onto the plane of $z = 0$.

When the line $(x, y, -\infty)$ to (x, y, ∞) does not penetrate through the vortex ring, $\varphi_{vr}^{+}(\boldsymbol{r})$ is equal to $\varphi_{vr}^{-}(\boldsymbol{r})$, otherwise they are different by a value of Γ.

The integral paths for the points N and S, as shown in Figure 3(a), should be chosen from (x, y, ∞) to (x, y, z) and from $(x, y, -\infty)$ to (x, y, z), respectively, to remove the potential jump at the two points. As for an arbitrary field point, the integral path should be chosen as a straight line, from the point (x, y, ∞) or $(x, y, -\infty)$ to (x, y, z), such that the line does not cross the bubble surface. With that, the remainder potential ϕ is a continuous function on the bubble ring.

The above criterion for choosing the integration path only works for the situation that the straight line from $(x, y, -\infty)$ or (x, y, ∞) intersects with the bubble surface at most two times. However, if a straight line from $(x, y, -\infty)$ or (x, y, ∞) intersects with the bubble surface for more than two times, the integration path is chosen as follows. First, a surface S_c enclosed by the vortex ring c and entirely within the bubble ring is chosen. The integral path is then chosen as a straight line, from the point (x, y, ∞) or $(x, y, -\infty)$ to (x, y, z), such that the line does not across the surface S_c.

D. Mesh control technique

The formulation is in the dimensionless form. At every time step, a particle at the bubble/free surface is upgraded using the prescribed velocity $\boldsymbol{v}_{pre}$ as follows:

$$\boldsymbol{v}_{pre}^{n+1}(\boldsymbol{r},t) = \boldsymbol{v}_{pre}^{n}(\boldsymbol{r},t) + \nabla_s \psi \left(\boldsymbol{r} + \boldsymbol{v}_{pre}^{n} t\right), \tag{3.14a}$$

$$\boldsymbol{v}_{pre}^{0}(\boldsymbol{r},t) = \boldsymbol{v}(\boldsymbol{r},t), \tag{3.14b}$$

where $\psi(\boldsymbol{r})$ is a function for the mesh control. The iteration in (3.14a) is performed to n. Note here that the normal component of the prescribed velocity is the same as that for the Lagrangian velocity, as such the prescribed velocity does not change the bubble shape but affects the mesh distribution.

One option is to choose $\psi(\boldsymbol{r})$ being proportion to the square of the local average mesh size $d_{mesh}(\boldsymbol{r})$,

$$\psi(\boldsymbol{r}) = \frac{\chi}{\Delta t} \frac{d_{mesh}^2(\boldsymbol{r})}{R_{eq}^2}, \tag{3.15}$$

where χ is a constant, R_{eq} is the equivalent radius of the bubble, and Δt is the time step. χ is chosen as 0.1 in the calculations performed. $\nabla_s \psi(\boldsymbol{r})$ is proportional to the mesh size and is along the direction that the mesh size increases most rapidly. Such a prescribed velocity makes mesh uniform. The factor $1/\Delta t$ is included to make the adjustment of mesh independent of time steps.

Another option to choose $\psi(\boldsymbol{r})$ is as follows:

$$\psi(\boldsymbol{r}) = \frac{\chi}{\Delta t} \frac{d_{mesh}^2(\boldsymbol{r})}{\rho_{cur}^2(\boldsymbol{r})}, \tag{3.16}$$

where $\rho_{cur}(\boldsymbol{r})$ is the curvature radius of the bubble/free surface. This operation generates a mesh with its mesh size being proportional to the curvature radius of the bubble surface.

When the jet impacts the opposite bubble surface, a surgical cut procedure is performed to change the fluid field into double-connected. We connect the second ring nodes of the jet tip and the nearest node on the opposite side together to generate a smoother toroidal eye with more divisions along the circular.

Before jet impact, the mesh of the jet front surface is usually finer than the opposite bubble surface, which is thus refined as follows. Suppose that node M and node N are the two impact points, and N is at the jet tip. Denote $\boldsymbol{r}_i^N$ $(i = 1, m)$ as the nodes on the second rings of the jet surface to the node N. Denote $\boldsymbol{r}_i^S$ as the nodes on the second rings of the opposite surface to the node M. Denote the nearest node on the opposite bubble surface to $\boldsymbol{r}_i^N$ as $\boldsymbol{r}_\mathrm{j}$ and denote the normal vector of the bubble surface at $\boldsymbol{r}_\mathrm{j}$ as $\boldsymbol{n}_\mathrm{j}$. The nodes $\boldsymbol{r}_i^S$ of the second ring of the opposite surface are adjusted as follows:

$$\boldsymbol{r}_i^{S_{new}} = \boldsymbol{r}_i^N + \boldsymbol{n}_j \left(\boldsymbol{r}_j - \boldsymbol{r}_i^N\right) \cdot \boldsymbol{n}_j. \tag{3.17}$$

IV. BIM MODELLING

A. Basic numerical model

The BIM model is grid-free in the flow domain and computationally efficient and is thus widely used in the field of bubble dynamics. It has been applied for an axisymmetric configuration for a bubble near a rigid boundary, a free surface, or a compliant surface (Lenoir, 1979; Blake *et al.*, 1986; Blake *et al.*, 1997; Brujan *et al.*, 2002; Pearson *et al.*, 2004b; Lind and Phillips, 2010; and Lind and Phillips, 2013) and for 3D configurations (Chahine and Harris, 1998a; Chahine and Harris, 1998b; and Klaseboer *et al.*, 2005b).

Linear planar triangular elements are used in the present BIM model. At each time step, we have a known bubble surface, a known free surface and known potential distributions on them. With this information, the tangential velocity on the two surfaces can be calculated from the gradient of the potential at the surfaces. The normal velocity at the two surfaces is obtained after solving the boundary integral equation (2.3). The bubble surface, free surface, and potential distributions on them are further updated by performing the Lagrangian time integration to (2.1c), (2.1e), and (2.1f), using a second-order Runge-Kutta scheme. A variable time step is chosen for accuracy and efficiency, in such a way that the maximum change of the potential in each time step is restricted by a constant (Blake *et al.*, 1986 and Blake *et al.*, 1987). The details on the numerical model using the BIM model for this problem can be found in Wang (1998), Wang and Manmi (2014), Wang *et al.* (2015), and Zhang and Liu (2015).

The moment when the liquid jet impacts its opposite surface requires special treatment during the simulation, the flow chart is shown in Figure 4. At the very motion when the jet penetration occurs, a local mesh refinement is executed at the jet tip and the opposite bubble surface. The mesh density near the impact zone is automatically controlled by using mesh control techniques as shown in Figures 2(c) and 2(d) with the segment lengths on both the second rings comparable after the mesh refinement.

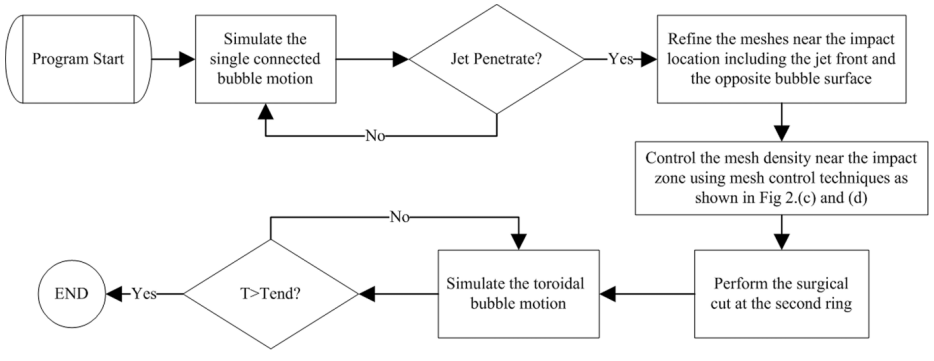

FIG. 4. Flow chart of the numerical scheme for modelling toroidal bubble dynamics.

B. Truncation of the infinite free surface

An infinite free surface has to be truncated in numerical simulations and this works well as long as the free surface is truncated sufficiently far away. However, a theoretical justification of the truncation is necessary. Green's function $G(\boldsymbol{r},\boldsymbol{q})$ in (2.4) can be expanded as

$$G(\boldsymbol{r},\boldsymbol{q}) = \frac{1}{r}\left(2 + (\boldsymbol{q}+\boldsymbol{q}')\cdot\frac{\boldsymbol{r}}{r^2}\right) + O\left(\frac{1}{r^3}\right). \tag{4.1}$$

Substitution in (2.3) yields

$$c(\boldsymbol{r},t)\,\varphi(\boldsymbol{r},t) = \frac{2}{r}\int\limits_{S_B+S_F}\frac{\partial\varphi(\boldsymbol{q},t)}{\partial n}dS + \frac{\boldsymbol{r}}{r^3}\cdot\int\limits_{S_B+S_F}\left(-2\boldsymbol{n}\varphi(\boldsymbol{q},t) - (\boldsymbol{q}+\boldsymbol{q}')\frac{\partial\varphi(\boldsymbol{q},t)}{\partial n}\right)dS + O\left(\frac{1}{r^3}\right). \tag{4.2}$$

We thus have $\varphi = O(1/r)$ and $\nabla\varphi = O\left(1/r^2\right)$; with these we know that at the free surface at far field, $n_z = O(1/r)$ and $\partial\varphi/\partial n = O\left(1/r^3\right)$, i.e.,

$$\varphi = O(1/r),\ \nabla\varphi = O\left(1/r^2\right);\ n_z = O(1/r),\ \partial\varphi/\partial n = O\left(1/r^3\right)\ \text{on } SF. \tag{4.3}$$

Oguz and Prosperetti (1989) and Robinson and Blak (2001) performed similar estimations using Havelock's theory (Havelock, 1942 and Havelock, 1955).

Denote the truncated free surface as S_{FT} and the truncated away free surface as S_{FF}. The boundary integral equation (2.3) can be written as follows:

$$c(\boldsymbol{r},t)\,\varphi(\boldsymbol{r},t) = \int\limits_{S_B+S_{FT}}\left(\frac{\partial\varphi(\boldsymbol{q},t)}{\partial n}G(\boldsymbol{r},\boldsymbol{q}) - \varphi(\boldsymbol{q},t)\frac{\partial G(\boldsymbol{r},\boldsymbol{q})}{\partial n}\right)dS(\boldsymbol{q}) + \beta, \tag{4.4}$$

where β can be estimated as follows using (4.1) and (4.3):

$$\beta = \int\limits_{S_{FF}}\left(\frac{\partial\varphi(\boldsymbol{q},t)}{\partial n}G(\boldsymbol{r},\boldsymbol{q}) - \varphi(\boldsymbol{q},t)\frac{\partial G(\boldsymbol{r},\boldsymbol{q})}{\partial n}\right)dS(\boldsymbol{q}) = \int\limits_{S_{FF}} O\left(\frac{1}{r^4}\right)dS = O\left(r_B^{-2}\right), \tag{4.5}$$

where $\boldsymbol{r}_B$ is the point on the external boundary of S_{FT} that is closest to the z-axis. The error associated with the truncation is thus at the order of $O\left(r_B^{-2}\right)$.

In the calculation performed, the bubble is meshed into 980 triangles. The truncated free surface takes a half circle shape with a radius 5 R_m, and is meshed into 3000 triangles with their sides varying gradually from 0.08 to 0.4 R_m, from near the bubble too far away, as illustrated in Figure 5(a). Our calculations show that the radius of the truncated area with a radius 5 R_m is sufficient. Figure 5(b) displays the results for a case characterized by $\varepsilon = 20$, $\delta = 0$, and $\gamma_f = 0.6$, with a truncated free surface having a radius 10 R_m, calculated using an axisymmetric BIM model (Wang *et al.*, 1996). The results are shown at jet impact, when the part of the free surface at 3 R_m away from the z-axis is almost flat.

C. Calculation of pressure field

With the flow field calculated from the BIM model, the pressure distribution can be calculated using the Bernoulli equation

$$\frac{p}{\rho} = \frac{p_\infty}{\rho} - \frac{\partial\varphi}{\partial t} - \frac{1}{2}|\nabla\varphi|^2 - g(z-d). \tag{4.6}$$

It is a well-known challenge to calculate the pressure field associated with bubble dynamics. To calculate $\dot{\varphi} = \partial\varphi/\partial t$ using the finite difference method often results in unaccepted errors due to very small time steps usually used for simulating a violent collapsing bubble. This is also because of flow instabilities associated with the jet impact and numerical instabilities due to the numerical treatment of the topological transition of the bubble shape. We calculate $\dot{\varphi}$ using the BIM model following Tanizawa (1995) and Wu (1998).

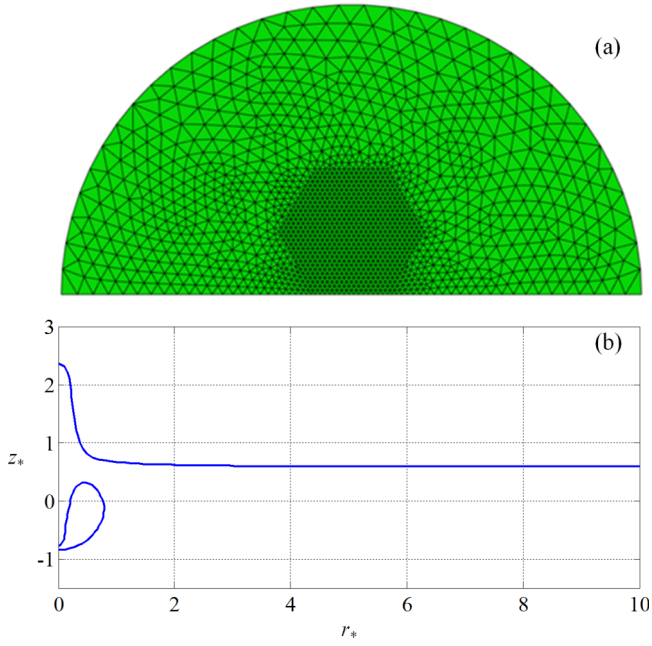

FIG. 5. (a) The truncated free surface takes a half circle shape with a radius 5 R_m and is meshed into 3000 triangles. (b) The bubble and free surface calculated using an axisymmetric BIM model for a case for $\varepsilon = 20$, $\delta = 0$, and $\gamma_f = 0.6$, with a truncated free surface having a radius 10 R_m.

It is easy to see that $\dot{\varphi}$ satisfies Laplace's equation. The boundary conditions for $\dot{\phi}$ on the rigid boundary and at far field can be obtained from (2.1b) and (2.1d) as follows:

$$\frac{\partial \dot{\varphi}}{\partial n} = 0 \text{ on } S_{\mathrm{W}}, \tag{4.7a}$$

$$\nabla \dot{\varphi} \to 0 \text{ as } \boldsymbol{r} \to \infty. \tag{4.7b}$$

As such, $\dot{\varphi}$ satisfies the same boundary integral equation as φ on the bubble surface and free surface as follows:

$$c(\boldsymbol{r},t)\,\dot{\varphi}(\boldsymbol{r},t) = \int_{S_B+S_F} \left(\frac{\partial \dot{\varphi}(\boldsymbol{q},t)}{\partial n} G(\boldsymbol{r},\boldsymbol{q}) - \dot{\varphi}(\boldsymbol{q},t) \frac{\partial G(\boldsymbol{r},\boldsymbol{q})}{\partial n} \right) dS(\boldsymbol{q}), \tag{4.8}$$

where $G(\boldsymbol{r},\boldsymbol{q})$ is the same Green function given in (2.4), which guarantees that $\dot{\varphi}$ satisfies the boundary conditions at the boundary and at infinity ((4.7a) and (4.7b)).

The boundary conditions for $\dot{\varphi}$ on the free surface and bubble surface can be obtained from (2.1e) and (2.1f) as follows:

$$\dot{\varphi} = -(\nabla\varphi \cdot \nabla)\varphi + \frac{1}{2}|\nabla\varphi|^2 - g z \text{ on } S_{\mathrm{F}}, \tag{4.9c}$$

$$\dot{\varphi} = -(\nabla\varphi \cdot \nabla)\varphi + \frac{1}{2}|\nabla\varphi|^2 - g(z-d) - \frac{p_B - p_\infty}{\rho} \text{ on } S_{\mathrm{B}}. \tag{4.9d}$$

With the distributions of $\dot{\varphi}$ on the free surface and bubble surface, $\dot{\varphi}_n$ on the two surfaces can be obtained by solving (4.8) using the BIM model. After that, one can calculate $\dot{\varphi}(\boldsymbol{r},t)$ at any field point $\boldsymbol{r}$ using (4.8) and calculate the pressure using (4.6).

The BIM approach for calculating $\dot{\varphi}_n$ almost doubles the CPU time of the model. However, the BIM equation and the boundary associated for $\dot{\varphi}$ are the same as that for φ; therefore the same influence matrix is used. The memory requirements and coding efforts for the approach are insignificant.

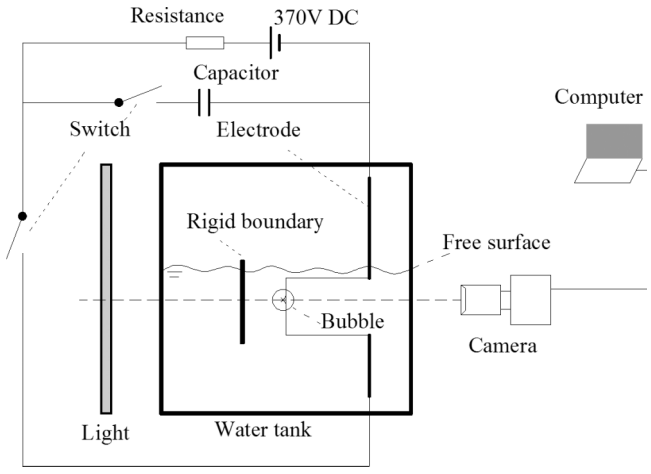

FIG. 6. Illustration of the experimental setup. A bubble is generated at a connect point of the thin copper wires extended from a capacitor. The interaction of the bubble and free surface is captured using a high speed camera at 20 000 FPS.

V. VALIDATION TO EXPERIMENT

To evaluate the numerical model, we carry out experiments for a bubble generated by low-voltage electric discharges in a cubic water tank with a side 0.5 m. The experimental setup is illustrated in Figure 6. A capacitor of 400 μF charged to 370 V is used to provide Joule's heating to generate bubbles. Thin copper wires extending from the capacitor are connected at a pre-decided position, where a bubble is to be generated. The evolution of the bubble and free surface is captured using a Phantom V12.1 high-speed camera at 20 000 frames per second (FPS), with illumination from a 2 kW spot light, opposite to the camera through a diffuser (matte glass). The rigid boundary is placed behind the bubble, which cannot be depicted in the figure; however, to illustrate its relative position to the bubble, the boundary is drawn between the bubble and the source of light. The copper wires are thin (with a radius 0.12 mm), compared to the bubble radius of about 10 mm; their influence on the bubble dynamics thus is small. The effects of the glass tank walls are negligible, as being more than 20 times the maximum bubble radius away from the bubble.

In numerical simulations comparing with the experiments, it is difficult to determine the initial pressure inside the spark generated bubble. Likely, it has been declared that the bubble's initial pressure, which is called the strength parameter ε in a dimensionless form, has little influence on the bubble motion when it is set as 100 and 500 (Blake *et al.*, 1998; Turangan *et al.*, 2006; and Li *et al.*, 2006). In this paper, we adopt $\varepsilon = 100$ for the numerical analysis which is widely used in the simulation of bubble motion in the dimensionless form except for a special case study at the end of this work.

Figure 7 shows the comparison between the experimental images and the numerical results for a spark generated bubble interacting with a free surface near a vertical boundary, characterized by $R_m = 12.5$ mm, $\gamma_f = 0.75$, and $\gamma_w = 1.4$. Buoyance effects are negligible in this case, since $\delta \approx 0.03$. The dimensionless initial bubble pressure for the computation is chosen as $\varepsilon = 100$. All the following features, observed in the experiment, are reproduced by the computation. The bubble first expands and the free surface rises (frames 7(a) and 7(b)), reaching its maximum volume in frame 7(b). The bubble then collapses, yet the free surface rises continuously, forming a high spike (frames 7(c)–7(e)). In the computational results, a jet forms and penetrates the bubble, towards the end of collapse (frames 7(d) and 7(e)). Although the jet cannot be seen in the experiment due to the opaqueness of the bubble surface, the bubble profiles of the computation agree well with the experiment at jet impact (frame 7(d)). After jet impact, a protrusion forms in the experimental image along the jet direction; nevertheless the main part of the bubble in the image agrees well with the computation. The bubble is apparently asymmetric, with the part proximity to the rigid boundary collapsing significantly slower than the distal side (frames 7(d) and 7(e)). A little difference appears in the comparison between experimental and numerical results in frame 7(e). The protrusion in

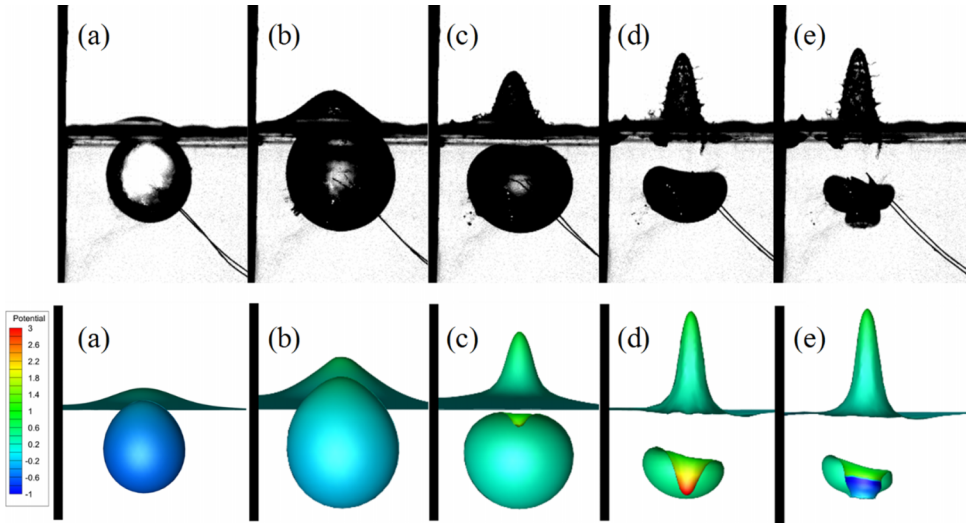

FIG. 7. Comparison between the experimental images (the upper row) and numerical results (the lower row) for the interaction of a spark generated bubble with a free surface near a vertical boundary (on the left side in each frame), for $R_m = 12.5$ mm, $\varepsilon = 100$, $\gamma_f = 0.75$, $\gamma_w = 1.4$, at $t = 0.471$, 0.941, 1.471, 1.824, 1.941 ms, for frames ((a)-(e)), respectively.

the numerical result is shorter than the experimental one due to the numerical smooth technique adopted in the program.

VI. INTERACTION OF BUBBLE/FREE SURFACE NEAR A VERTICAL BOUNDARY

Figure 8 shows the case for a vertical boundary without the buoyancy effects for $\gamma_f = 0.8$ and $\gamma_w = 1.5$, where the bubble is closer to the free surface than to the boundary. While the bubble

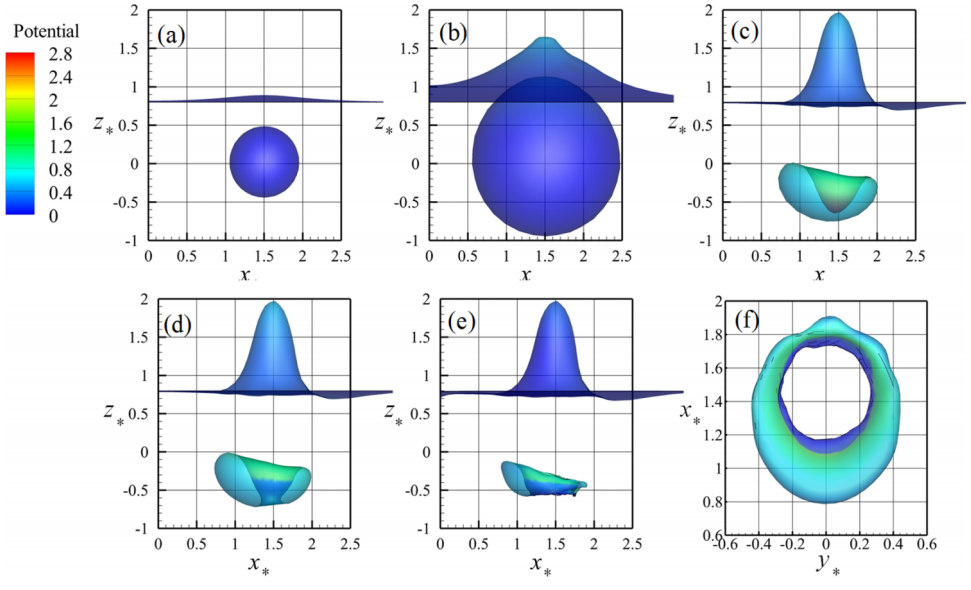

FIG. 8. Interaction of a bubble with a free surface near a vertical boundary for $\gamma_f = 0.8$ and $\gamma_w = 1.5$, at the dimensionless times t_*: (a) 0.09, (b) 0.75, (c) 1.53, (d) 1.54, and (e) 1.60, respectively. (f) The top view of the bubble ring shown in Figure 7(e), just before it breaks down to become a crescent shaped bubble.

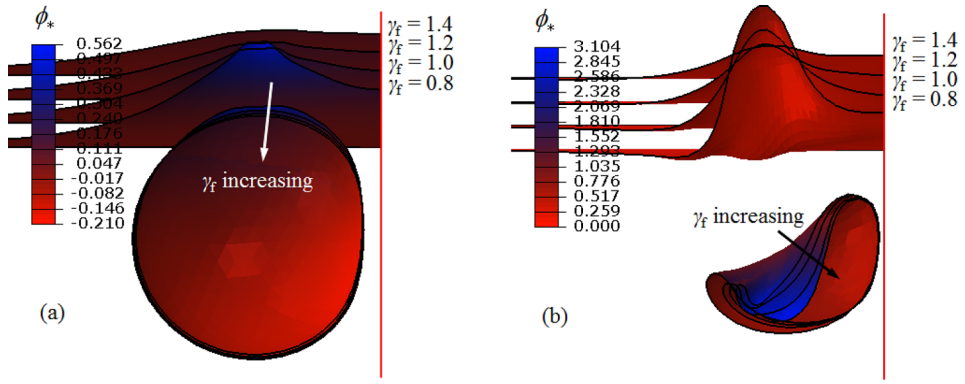

FIG. 9. Comparison of the profiles of the bubble surface and free surface at (a) the maximum bubble volume and (b) jet impact, for their interaction near a vertical boundary, for $\gamma_w = 1.0$ and $\gamma_f = 0.8$, 1.0, 1.2, 1.4, respectively.

expands (Figures 8(a) and 8(b)) and collapses (Figures 8(b) and 8(c)), the free surface rises continuously, forming a high spike (Figure 8(c)). A downward jet forms due to the repulsion of the free surface (Figure 8(c)), and the bubble becomes significantly asymmetric.

After jet impact (Figure 8(d)), a vortex ring is put inside the bubble. The bubble becomes a bubble ring and continues collapsing asymmetrically, whose cross section is much thinner at the distal side from the boundary (Figures 8(d) and 8(e)). Figure 8(f) displays the top view of the bubble ring just before its breaking. Afterwards it will become a crescent shaped bubble and the fluid domain returns to be singly connected.

Parametric studies are carried out in terms of γ_f and γ_w, respectively. Figure 9 shows the profiles of the bubble surface and free surface for fixed $\gamma_w = 1.0$ and various $\gamma_f = 0.8$, 1.0, 1.2, and 1.4, respectively. As the bubble is initiated deeper, the features for the bubble expansion do not change significantly: its nearer side to the boundary becomes flattened near the end of expansion. However, bubble behaviours during collapse depend obviously on its depth. The bubble collapses faster on the distal side from the boundary. This trend is strengthened while the bubble is initiated deeper, when the repulsion due to the free surface decreases, and the attraction due to the boundary becomes relatively strong.

As for the free surface, the height of the free surface hump at the end of expansion decreases with the bubble depth; the free surface between the bubble and boundary becomes flatten for $\gamma_f > \gamma_w$. At the end of collapse, a sharp free surface spike forms for $\gamma_f = 0.8$, its height decreases significantly with γ_f, and the elevation of the free surface between the spike and boundary decreases slowly with γ_f.

Figure 10 shows the time histories of (a) the x-component x_{cen} and (b) z-component z_{cen} of the bubble centroid, respectively, for the cases in Figure 9. The bubble first rises to the free surface and leaves from the boundary, moves back before the end of expansion, and moves down and towards the boundary rapidly at the end of collapse. As the bubble is initiated deeper, the horizontal

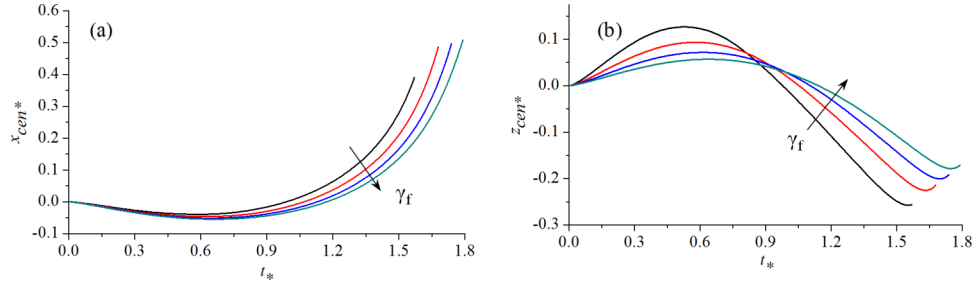

FIG. 10. Time histories of (a) the x-component x_{cen^*} and (b) z-component z_{cen^*} of the bubble centroid for the cases in Figure 9.

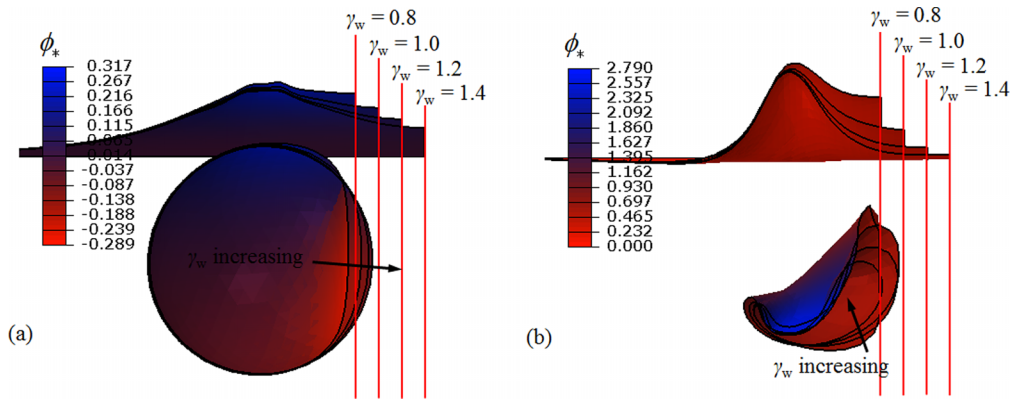

FIG. 11. Comparison of the profiles of the bubble surface and free surface at (a) the maximum bubble volume and (b) jet impact for their interaction near a vertical boundary, for $\gamma_f = 1.0$ and $\gamma_w = 0.8$, 1.0, 1.2, 1.4, respectively.

central movement increases and the vertical central movement decreases. The bubble migrates more vertically than horizontally during expansion but migrates much more horizontally during collapse.

Figure 11 shows the profiles of the bubble surface and free surface for fixed $\gamma_f = 1.0$ and various $\gamma_w = 0.8$, 1.0, 1.2, 1.4, respectively. As $\gamma_w \leq 1.0$, the bubble surface proximity to the boundary is flattened at the end of expansion. The boundary effects on the bubble dynamics are insignificant at $\gamma_w = 1.4$ till the end of expansion, when the bubble is approximately symmetric. However, significant boundary effects display during collapse: the nearer side of the bubble surface to the boundary remains in contact with the boundary as $\gamma_w \leq 1.0$, is attracted by the boundary as $\gamma_w > 1.0$, and collapses slower than the distal side. The asymmetric effects are strengthened at a smaller γ_w.

The closeness of the bubble to the boundary does not affect the height of the free surface hump significantly but affects the free surface profile. As $\gamma_w \leq 1.0$, the free surface between the hump and boundary rises up resulting in a plateau because the nearer side of the bubble to the boundary is flattened by the boundary, since the later stage of expansion. The free surface plateau disappears as $\gamma_w > 1.0$, and the boundary effects on the free surface are not appreciable for $\gamma_w \geq 1.4$.

Figure 12 shows the time histories of the bubble centroid (x_{cen}, z_{cen}). The bubble again first rises to the free surface and leaves away from the boundary slightly, moves back before reaching its maximum volume, and moves rapidly at the end of collapse. As the bubble is initiated closer to the boundary, the horizontal central movement increases, and the vertical central movement decreases, since the bubble is attracted by a stronger boundary attraction.

VII. INTERACTION OF BUBBLE/FREE SURFACE NEAR AN INCLINED BOUNDARY

Consider the interaction of a bubble with a free surface, near a flaring boundary with an inclined angle $\alpha = -10°$, for $\gamma_w = 1.0$ and $\gamma_f = 1.0$. Figure 13 shows the profiles of the bubble

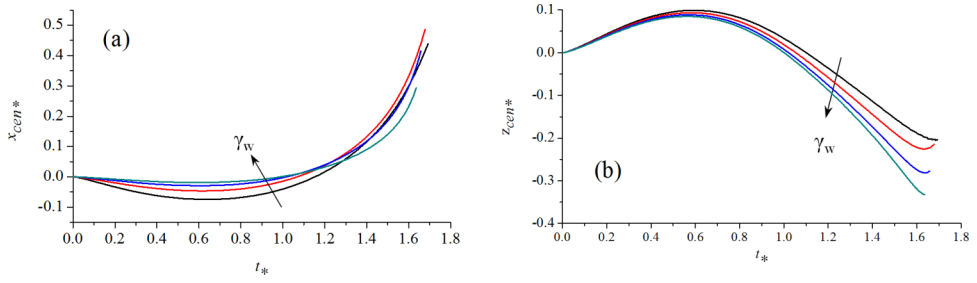

FIG. 12. Time histories of (a) the x-component x_{cen^*} and (b) z-component z_{cen^*} of the bubble centroid, for the cases in Figure 11.

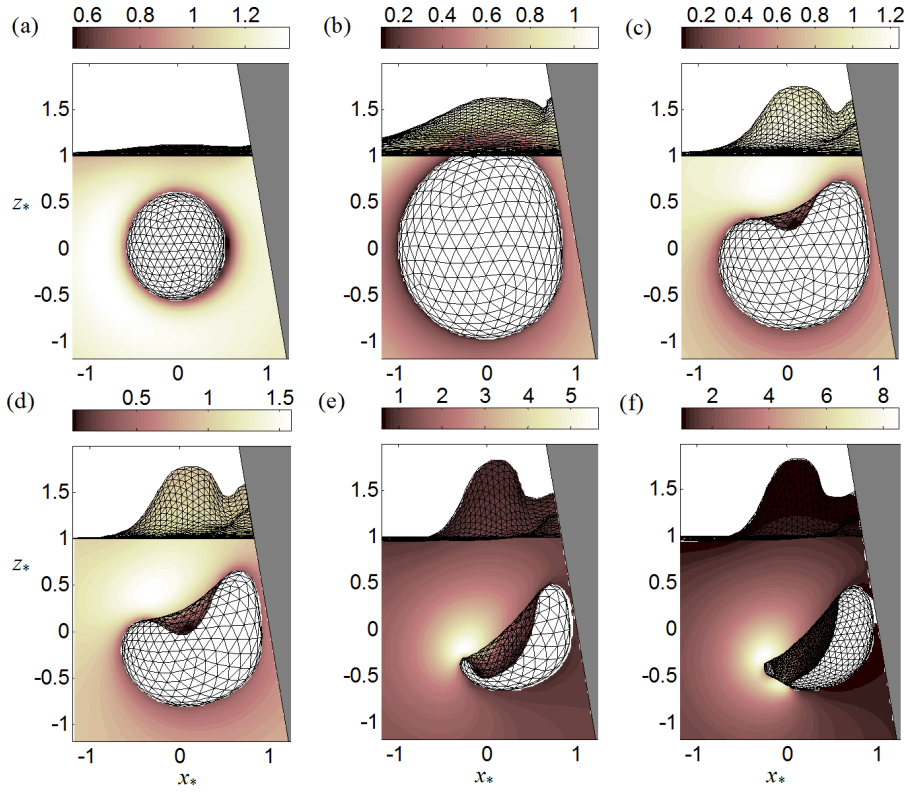

FIG. 13. Interaction of a bubble with a free surface near a flaring boundary, for $\gamma_w = 1.0$, $\gamma_f = 1.0$, and $\alpha = -10°$, at typical dimensionless times t_*: (a) 0.15, (b) 0.77, (c) 1.32, (d) 1.50, (e) 1.67, and (f) 1.68. Contours of the pressure of the flow field are also shown in the figure.

surface and free surface at typical time steps, as well as the contours for the dimensionless pressure. In the middle of expansion (Figure 13(a)), the pressure of the bubble gases is lower than the surrounding liquid; however, the bubble continues expanding due to inertial. At the maximum bubble volume (Figure 13(b)), the bubble surface proximity to the boundary is flattened due to the boundary, and a side hump of the free surface forms near its intersection with the boundary, raised by the high pressure zone observed there in Figures 13(a) and 13(b).

During collapse (Figures 13(c) and 13(d)), a high pressure zone occurs between the top of the bubble surface and the free surface, which drives a free surface spike and a downward bubble jet simultaneously. The side hump near the boundary becomes more prominent. At the end of collapse (Figure 13(e)), a free surface spike forms above the bubble, the high pressure zone shifts towards the distal side of the bubble from the boundary due to the boundary effects, and a large jet forms with its direction rotating towards the boundary. Then the bubble is penetrated by the jet (Figure 13(f)).

We next consider the interaction near a fall in boundary for $\alpha = 10°$, with the remaining parameters being the same as in Figure 13. The general features of this case are similar to that for a flaring boundary in Figure 13. The bubble surface proximity to the boundary is flattened due to the boundary at the end of expansion. A high pressure zone is generated between the top of the bubble surface and the free surface subsequently, which drives an upward free surface hump and a downward bubble jet. At the end of collapse, the high pressure zone shifts to the distal side of the bubble from the boundary, and the jet rotates to the direction pointing to the boundary.

However the free surface motion near a fall in boundary displays different features. The upward velocity at the free surface near the boundary is relatively smaller than elsewhere during expansion (Figure 14(a)); the elevation of the free surface is lower near the boundary at the end of expansion (Figure 14(b)). During collapse, a free surface trough develops near the intersection, as the fluid is pulled towards the contracting bubble (Figures 14(c)–14(e)).

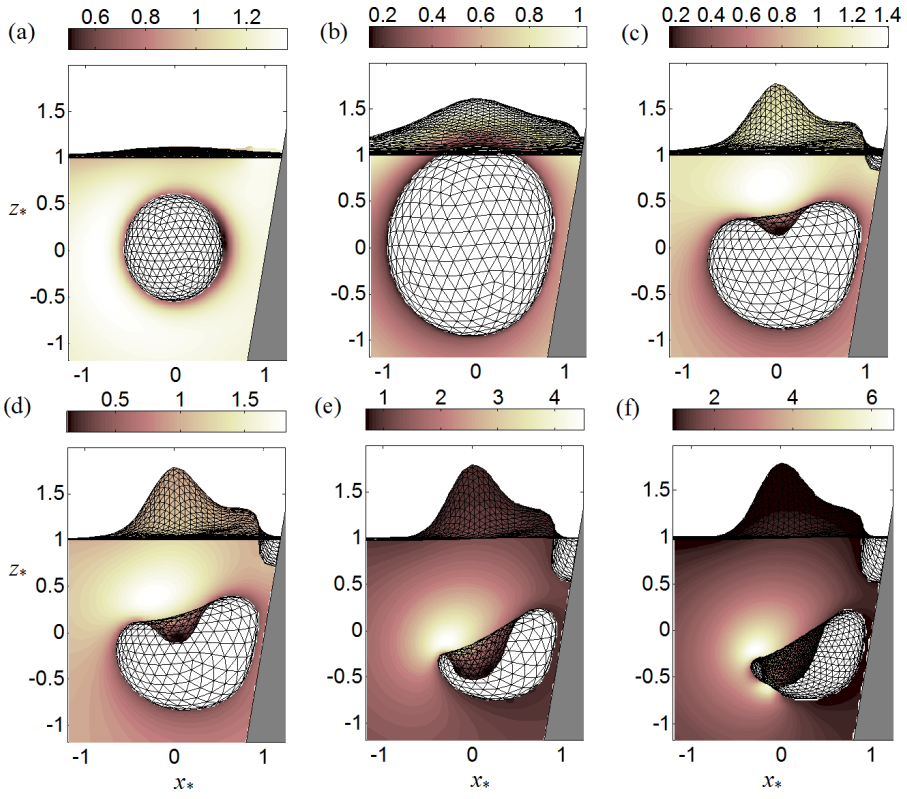

FIG. 14. Interaction of a bubble with a free surface near a fall in boundary for $\gamma_w = 1.0, \gamma_f = 0.8$, and $\alpha = 10°$, at the typical dimensionless times t_*: (a) 0.15, (b) 0.77, (c) 1.40, (d) 1.50, (e) 1.67, and (f) 1.68, respectively. Contours of the pressure of the field are also shown in the figure.

We now perform a parametric study for the inclined angle for $\alpha = -10°$, $0°$, $10°$, respectively, with the other parameters fixed at $\gamma_f = 1.0$ and $\gamma_w = 1.0$. As shown in Figure 15, the bubble takes similar shapes so does the free surface hump both at the maximum bubble volume (Figure 15(a)) and at jet impact (Figure 15(b)). However, the free surface near the boundary displays different features associated with the inclined angle of the boundary. The elevation of the free surface

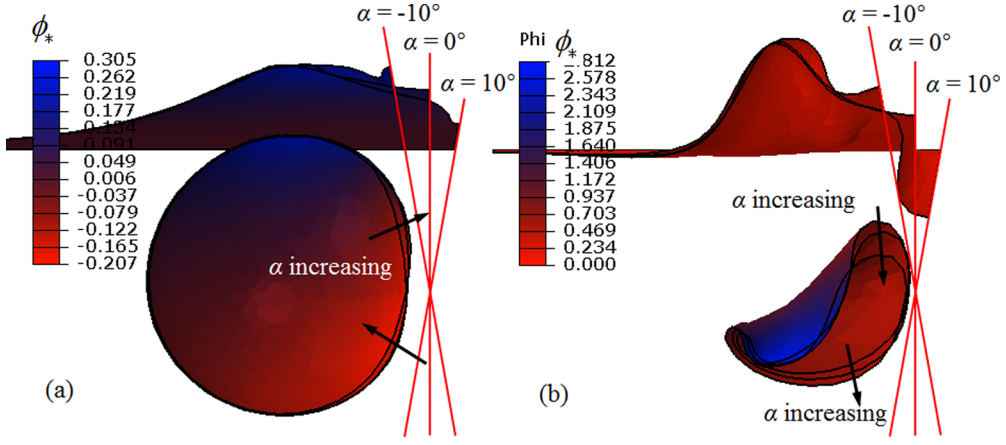

FIG. 15. Comparison of the profiles of the bubble surface and free surface, for various inclined angles of the boundary $\alpha = -10°$, $0°$, $10°$, respectively at (a) the maximum bubble volume (left) and (b) jet impact (right). The other parameters for the cases are $\delta = 0, \gamma_w = 1.0$, and $\gamma_f = 1.0$, respectively.

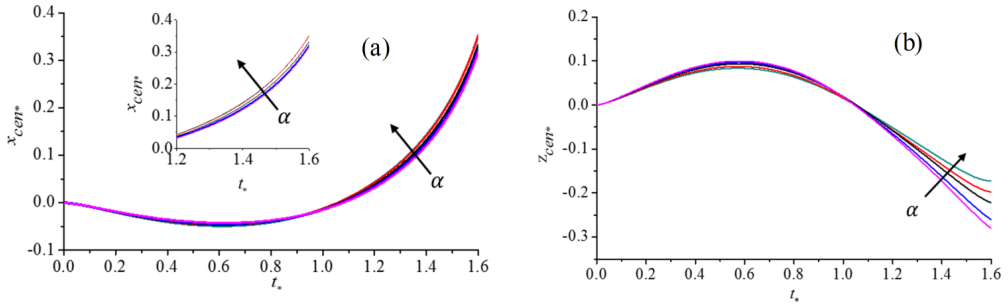

FIG. 16. Time histories of (a) the x-component x_{cen^*} and (b) z-component z_{cen^*} of the bubble centroid versus the inclined angle α of the boundary for the cases in Figure 16.

between the hump and boundary decreases with α, a side hump of the free surface forms near a flaring boundary at $\alpha = -5°$ and $-10°$, whereas a trough forms near a fall in boundary at $\alpha = 5°$ and $10°$.

Figure 16 shows the time histories of the x- and z-components of the bubble centroid versus α for the cases in Figure 15. An interesting feature displayed is that the lateral translation towards the boundary does not change with α appreciably; however, the vertical translation decreases with α. A bubble migrates deeper besides a flaring boundary than a fall in boundary.

The mechanism for this phenomenon is illustrated in Figure 17. The Bjerknes force from the boundary $\boldsymbol{F}_w$ is pointing perpendicular to the boundary, and the Bjerknes force due to the free surface $\boldsymbol{F}_f$ is downwards. As such the total force $\boldsymbol{F}$ acting on the bubble, including the buoyancy $\boldsymbol{F}_b$, is estimated as follows along the x- and z-axes, respectively:

$$F_x = F_w \cos\alpha = F_w\left(1 - \frac{1}{2}\alpha^2\right) + O\left(\alpha^3\right), \tag{7.1}$$

$$F_z = F_b - F_f + F_w \sin\alpha = F_b - F_f + F_w\alpha + O\left(\alpha^3\right). \tag{7.2}$$

As α is small, the change in F_x due to α is at $O(\alpha^2)$, whereas the change in F_y is linear in α.

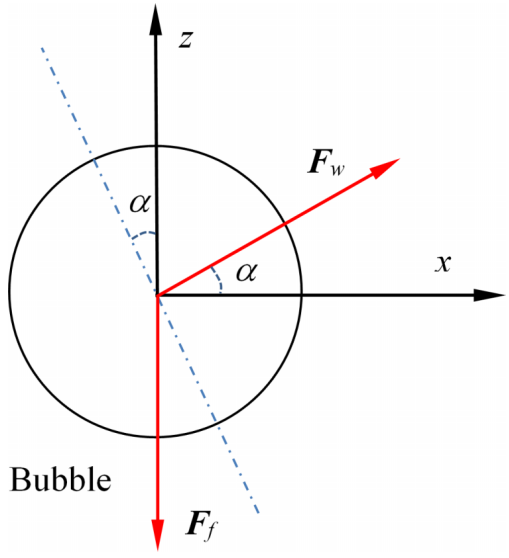

FIG. 17. Illustration of the downward Bjerknes force $\boldsymbol{F}_f$ due to the free surface and the Bjerknes force $\boldsymbol{F}_w$ due to the boundary pointing perpendicular to the boundary.

VIII. INTERACTION OF LARGE SCALE BUBBLE/FREE SURFACE NEAR AN INCLINED BOUNDARY

Bubbles associated with underwater explosions and airgun operations have large radii of $O(1)$ m or larger, which are usually subject to significant buoyancy effects. We consider an underwater explosion bubble due to 200 kg TNT, exploded at a depth of 7.6 m, and at a standoff distance of 7.6 m from a boundary. The maximum bubble radius for this case is 7.6 m. The corresponding dimensionless parameters are $R_0 = 0.089, \varepsilon = 416, \delta = 0.66, \gamma_w = 1.0$, and $\gamma_f = 1.0$, respectively. Three inclined angles of the boundary are considered for $\alpha = -10°$, 0°, and 10°, respectively.

Figure 18 shows the profiles of the bubble surface and free surface at typical time steps, which display similar features at the end of expansion (Figure 18(a)) as the cases without buoyancy (Figure 15(a)), except that the free surface hump is higher and a larger part of the bubble has risen above the original calm water surface. The buoyancy effects become prominent during collapse. During the middle stage of collapse (Figure 18(b)), two counter jets start to form due to the free surface repulsion and buoyancy, respectively. The two jets develop subsequently, impact each other (Figure 18(c)), and a toroidal bubble forms (Figure 18(d)).

As compared to the cases without buoyancy (Figure 15), the asymmetric features of collapse are strengthened, and a larger part of the bubble surface is attracted by the Bjerknes force of the boundary (Figure 18(c)). This is because the repellence due to the free surface is partially balanced by buoyancy, and the boundary attraction becomes relatively stronger.

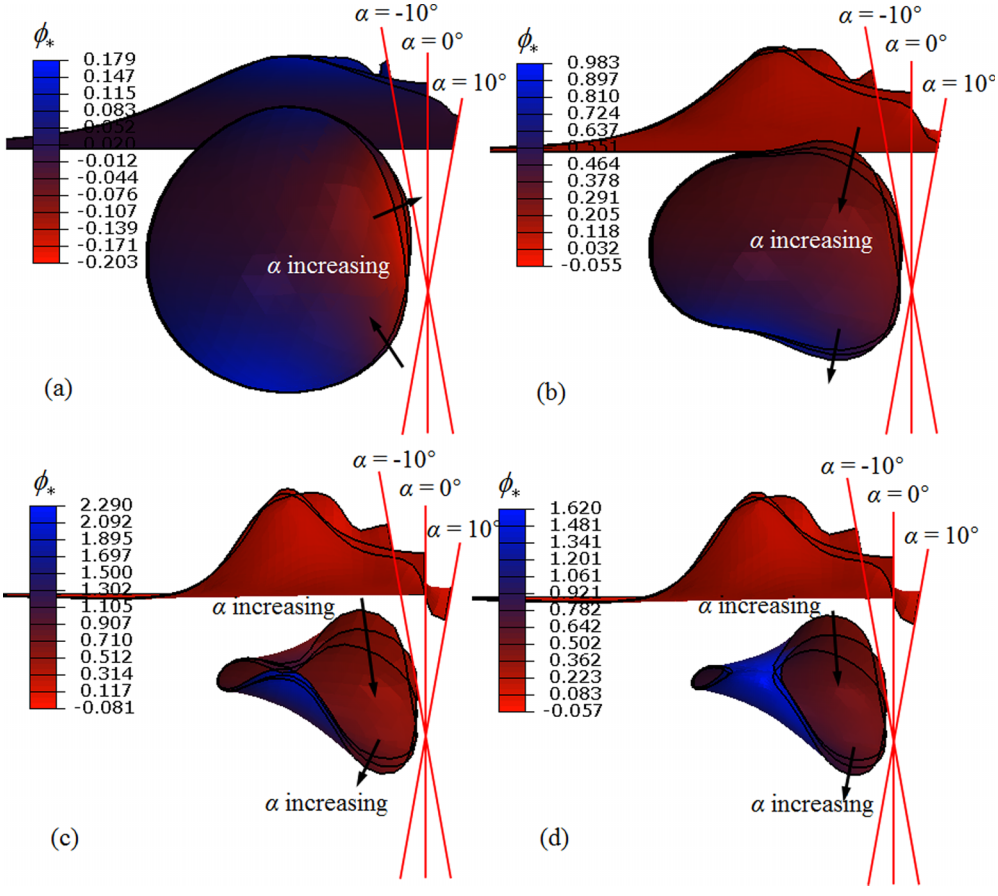

FIG. 18. Interaction of an underwater explosion bubble with a free surface near an inclined wall, with inclined angles $\alpha = -10°$, 0°, and 10°, respectively, at dimensionless time t_*: (a) 0.90 (at the maximum volume), (b) 1.30, (c) 1.59 (jet impact), and (d) 1.60 (during the toroidal phase). Other dimensionless parameters for the cases are $R_{0^*} = 0.089, \varepsilon = 416, \delta = 0.66, \gamma_w = 1.0$, and $\gamma_f = 1.0$, respectively.

The singular features of the free surface at the intersection with the boundary exist as well, when subject to buoyancy. A side trough occurs as the bubble near a fall in boundary for $\alpha = 10°$, which develops continuously during collapse. A side hump appears as the bubble near a flaring boundary for $\alpha = -10°$, which is a well know phenomenon associated with underwater explosion bubble dynamics near a hull.

IX. SUMMARY AND CONCLUSIONS

Three dimensional toroidal bubble dynamics are simulated based on the boundary integral method (BIM) coupled with a new impact model and a vortex ring model, enabling a smooth transition from a singly connected bubble to a toroidal bubble. We show that the potential due to a vortex ring can be reduced to the line integral along the vortex ring. The pressure distribution in the flow field is calculated by using the Bernoulli equation, where the partial derivative of the velocity potential in time is calculated using the BIM model to avoid numerical instabilities. Experiments are carried out for a spark generated bubble interacting with a free surface near a boundary, which is captured by using a high speed camera. Our numerical results agree well with the experimental images for the bubble and free surface shapes. Some new features for the interaction of a transient bubble with a free surface near an inclined boundary are as follows.

A high pressure zone is generated between the bubble surface and free surface, since the early stage of collapse, which drives a free surface spike and a downward bubble jet simultaneously, as the bubble collapsing. Towards the end of collapse, the high pressure zone shifts towards the distal side of the bubble away from the boundary, causing the jet rotating towards the boundary. The distal side of the bubble collapses faster and the nearer side of the bubble is attracted by the boundary. After jet impact, an asymmetric bubble ring forms, with a relatively small cross section at the distal side, where it breaks subsequently, becoming a crescent shaped bubble.

As the inclined angle of the boundary increases, the horizontal migration of the bubble does not change appreciably, but it migrates deeper besides a flaring boundary than a fall in boundary. The free surface near the boundary displays special features: The elevation of the free surface between the free surface spike and boundary decreases with the inclined angle, a side hump forms near a flaring boundary, and a trough of the free surface forms near a fall in boundary.

Buoyancy effects are appreciable for a large bubble, the Bjerknes repellence acting on the bubble due to the free surface is countervailed partially by buoyancy, and the Bjerknes attraction due to the boundary becomes relatively stronger. As a result, the asymmetric collapse due to the boundary is strengthened, and a larger part of the bubble surface is attracted by the boundary during collapse.

ACKNOWLEDGMENTS

This work is supported by the National Natural Science Foundation of China (Grant Nos. 51379039, 11672082, and 51609044). The authors would like to express sincere thanks to Professor John R. Blake for his valuable comments on the manuscript.

Barker, D. and Landrø, M., "An alternative method for modeling close-range interactions between air guns," Geophysics **79**, 1–7 (2014).

Best, J. P., "The formation of toroidal bubbles upon collapse of transient cavities," J. Fluid. Mech. **251**, 79–107 (1993).

Best, J. P. and Blake, J. R., "An estimate of the Kelvin impulse of a transient cavity," J. Fluid. Mech. **261**, 75–93 (1994).

Best, J. P. and Kucera, A., "A numerical investigation of non-spherical rebounding bubbles," J. Fluid Mech. **245**, 137–191 (1992).

Blake, J. R. and Gibson, D. C., "Cavitation bubbles near boundaries," Annu. Rev. Fluid. Mech. **19**, 99–123 (1987).

Blake, J. R., Hooton, M. C., Robinson, P. B., and Tong, P. R., "Collapsing cavities, toroidal bubbles and jet impact," Philos. Trans. R. Soc. A **355**, 537–550 (1997).

Blake, J. R., Keen, G. S., Tong, R. P., and Wilson, M., "Acoustic cavitation: The fluid dynamics of non–spherical bubbles," Philos. Trans. R. Soc. A **357**, 251–267 (1999).

Blake, J. R., Taib, B. B., and Doherty, G., "Transient cavities near boundaries. I. Rigid boundary," J. Fluid. Mech. **170**, 479–497 (1986).

Blake, J. R., Taib, B. B., and Doherty, G., "Transient cavities near boundaries. II. Free surface," J. Fluid. Mech. **181**, 197 (1987).

Blake, J. R., Tomita, Y., and Tong, R. P., "The art, craft and science of modelling jet impact in a collapsing cavitation bubble," Appl. Sci. Res. **58**, 77–90 (1998).
Bonometti, T. and Magnaudet, J., "Transition from spherical caps to toroidal bubbles," Phys. Fluids **18**, 052102 (2006).
Bonometti, T. and Magnaudet, J., "An interface-capturing method for incompressible two-phase flows. Validation and application to bubble dynamics," Int. J. Multiphase Flow **33**, 10 (2007).
Brennen, C. E., *Cavitation and Bubble Dynamics* (Oxford University Press, New York, Oxford, 1995).
Brujan, E. A., Keen, G. S., Vogel, A., and Blake, J. R., "The final stage of the collapse of a cavitation bubble close to a rigid boundary," Phys. Fluids **14**, 85 (2002).
Caldwell, J., "Does air-gun noise harm marine mammals?," Leading Edge **21**, 75–76 (2002).
Chahine, G. L. and Bovis, A., "Oscillation and collapse of a cavitation bubble in the vicinity of a two-liquid interface," in *Presented at Cavitation and Inhomogeneities in Underwater Acoustics* (Springer-Verlag, New York, 1980).
Chahine, G. L. and Harris, G., *Multi-Cycle Underwater Explosion Bubble Model. Part I: Theory and Validation Examples for Free-Field Bubble Problems* (U.S. Naval Surface Warfare Center Indian Head Division, 1998a).
Chahine, G. L. and Harris, G., *Multi-Cycle Underwater Explosion Model. Part II: Validation Examples for Hull Girder Whipping Problems* (U.S. Naval Surface Warfare Center Indian Head Division, 1998b).
Chahine, G. L. and Perdue, T. O., "Simulation of the three-dimensional behaviour of an unsteady large bubble near a structure," AIP Conf. Proc. **197**, 188–199 (1990).
Chen, Y., Liu, L., Ge, H., Liu, B., and Qiu, X., "Using an airgun array in a land reservoir as the seismic source for seismotectonic studies in Northern China: Experiments and preliminary results," Geophys. Prospect. **56**, 601–612 (2008).
Cole, R. H., *Underwater Explosion* (Princeton University Press, Princeton, USA, 1948).
Cox, E., Pearson, A., Blake, J. R., and Otto, S. R., "Comparison of methods for modelling the behaviour of bubbles produced by marine seismic airguns," Geophys. Prospect. **52**, 451–477 (2004).
Curtiss, G. A., Leppinen, D. M., Wang, Q. X., and Blake, J. R., "Ultrasonic cavitation near a tissue layer," J. Fluid. Mech. **730**, 245–272 (2013).
Feng, Z. C. and Leal, L. G., "Nonlinear bubble dynamics," Annu. Rev. Fluid. Mech. **29**, 201–243 (1997).
Fernandez Rivas, D., Stricker, L., Zijlstra, A. G., Gardeniers, H. J. G. E., Lohse, D., and Prosperetti, A., "Ultrasound artificially nucleated bubbles and their sonochemical radical production," Ultrason. Sonochem. **20**, 510–524 (2013).
Han, B., Köhle, K., Jungnickel, K., Mettin, R., Lauterborn, W., and Vogel, A., "Dynamics of laser-induced bubble pairs," J. Fluid. Mech. **771**, 706–742 (2015).
Havelock, T. H., "The damping of the heaving and pitching motion of a ship," London, Edinburgh Dublin Philos. Mag. J. Sci. **33**, 666–673 (1942).
Havelock, T. H., "Waves due to a floating sphere making periodic heaving oscillations," Proc. R. Soc. A **231**, 1–7 (1955).
Hsiao, C. T., Choi, J. K., Singh, S., Chahine, G. L., Hay, T. A. *et al.*, "Modelling single- and tandem-bubble dynamics between two parallel plates for biomedical applications," J. Fluid. Mech. **716**, 137–170 (2013).
Hsiao, C.-T., Jayaprakash, A., Kapahi, A., Choi, J.-K., and Chahine, G. L., "Modelling of material pitting from cavitation bubble collapse," J. Fluid. Mech. **755**, 142–175 (2014).
Huang, B., Young, Y., Wang, G., and Shyy, W., "Combined experimental and computational investigation of unsteady structure of sheet/cloud cavitation," J. Fluids Eng. **135**(7), 071301 (2013).
Hung, C. F. and Hwangfu, J. J., "Experimental study of the behaviour of mini-charge underwater explosion bubbles near different boundaries," J. Fluid. Mech. **651**, 55–80 (2010).
Jayaprakash, A., Chao-Tsung, H., and Chahine, G., "Numerical and experimental study of the interaction of a spark-generated bubble and a vertical wall," J. Fluids Eng. **134**, 031301 (2012).
Jayaprakash, A., Singh, S., and Chahine, G., "Experimental and numerical investigation of single bubble dynamics in a two-phase bubbly medium," J. Fluids Eng. **133**, 121305 (2011).
Ji, B., Luo, X. W., and Wu, Y. L., "Unsteady cavitation characteristics and alleviation of pressure fluctuations around marine propellers with different skew angles," J. Mech. Sci. Technol. **28**(4), 1339–1348 (2014).
Klaseboer, E., Hung, K. C., Wang, C. W., and Khoo, B. C., "Experimental and numerical investigation of the dynamics of an underwater explosion bubble near a resilient/rigid structure," J. Fluid. Mech. **53**, 387–413 (2005a).
Klaseboer, E., Khoo, B. C., and Hung, K. C., "Dynamics of an oscillating bubble near a floating structure," J. Fluid. Struct. **10**, 1–10 (2005b).
Lauterborn, W. and Kurz, T., "Physics of bubble oscillations," Rep. Prog. Phys. **73**, 106501 (2010).
Lauterborn, W., Kurz, T., Mettin, R., and Ohl, C. D., "Experimental and theoretical bubble dynamics," Adv. Chem. Phys. **110**, 295–380 (1999).
Lauterborn, W. and Vogel, A., "Shock wave emission by laser generated bubbles," in *Bubble Dynamics and Shock Waves*, edited by Delale, C. F. (Springer, Berlin, Heidelberg, 2013), pp. 67–103.
Leighton, T. G., *The Acoustic Bubble* (Academic Press, 1994).
Lenoir, M., "A calculation of the parameters of the high-speed jet formed in the collapse of a bubble," J. Appl. Mech. Tech. Phys. **20**, 333–337 (1979).
Li, S., Han, R., and Zhang, A. M., "Nonlinear interaction between a gas bubble and a suspended sphere," J. Fluid. Struct. **65**, 333–354 (2006).
Lind, S. J. and Phillips, T. N., "The effect of viscoelasticity on a rising gas bubble," J. Non-Newtonian Fluid Mech. **165**, 852–865 (2010).
Lind, S. J. and Phillips, T. N., "The effect of viscoelasticity on the dynamics of gas bubbles near free surfaces," Phys. Fluids **25**, 022104 (2013).
Liu, Y. L., Wang, Y., and Zhang, A. M., "Interaction between bubble and free surface near vertical wall with inclination," Acta Phys. Sin. **62**, 214703 (2013).
Madsen, P. T., Johnson, M., Miller, P. J., Aguilar Soto, N., Lynch, J., and Tyack, P., "Quantitative measures of air-gun pulses recorded on sperm whales (Physeter macrocephalus) using acoustic tags during controlled exposure experiments," J. Acoust. Soc. Am. **120**, 2366–2379 (2006).

Magnaudet, J. and Eames, I., "The motion of high-Reynolds-number bubbles in inhomogeneous flows," Annu. Rev. Fluid Mech. **32**, 659–708 (2000).
Milne-Thompson, L. M., *Theoretical Hydrodynamics* (Macmillan Co., New York, 1968).
Oguz, H. and Prosperetti, A., "Surface-tension effects in the contact of liquid surfaces," J. Fluid. Mech. **203**, 149–171 (1989).
Ohl, C.-D., Arora, M., Ikink, R., de Jong, N., Versluis, M. *et al.*, "Sonoporation from jetting cavitation bubbles," Biophys. J. **91**, 4285–4295 (2006).
Pearson, A., Blake, J. R., and Otto, S. R., "Jets in bubbles," J. Eng. Math. **48**, 391–412 (2004a).
Pearson, A., Cox, E., Blake, J. R., and Otto, S. R., "Bubble interactions near a free surface," Eng. Anal. Boundary Elem. **28**, 295–313 (2004b).
Plesset, M. S. and Prosperetti, A., "Bubble dynamics and cavitation," Annu. Rev. Fluid. Mech. **9**, 145–185 (1977).
Rayleigh, Lord, "On the pressure developed in a liquid during the collapse of a spherical cavity," Philos. Mag. **34**, 94–98 (1917).
Robinson, P. B. and Blak, J. R., "Interaction of cavitation bubbles with a free surface," J. Appl. Phys. **89**, 8225–8237 (2001).
Song, W. D., Hong, M. H., Lukyanchuk, B., and Chong, T. C., "Laser-induced cavitation bubbles for cleaning of solid surfaces," J. Appl. Phys. **95**, 2952–2956 (2004).
Szeri, A. J., Storey, B. D., Pearson, A., and Blake, J. R., "Heat and mass transfer during the violent collapse of nonspherical bubbles," Phys. Fluids **15**, 2576–2586 (2003).
Tanizawa, K., "A nonlinear simulation method of 3-D body motions in waves (1st report): Formulation of the method with acceleration potential," J. Soc. Nav. Archit. Jpn. **1995**, 179–191.
Turangan, C. K., Ong, G. P., Klaseboer, E., and Khoo, B. C., "Experimental and numerical study of transient bubble-elastic membrane interaction," J. Appl. Phys. **100**, 054910 (2006).
Wang, C., Khoo, B. C., and Yeo, K. S., "Elastic mesh technique for 3D BIM simulation with an application to underwater explosion bubbles," Comput. Fluids **32**, 1195–1212 (2003).
Wang, Q. X., "The evolution of a gas bubble near an inclined wall," Theor. Comput. Fluid Dyn. **12**, 29–51 (1998).
Wang, Q. X., "Numerical simulation of violent bubble motion," Phys. Fluids **16**, 1610–1619 (2004).
Wang, Q. X., "Non-spherical bubble dynamics of underwater explosions in a compressible fluid," Phys. Fluids **25**, 072104 (2013).
Wang, Q. X. and Blake, J. R., "Non-spherical bubble dynamics in a compressible liquid. I. Travelling acoustic wave," J. Fluid. Mech. **659**, 191–224 (2010).
Wang, Q. X. and Blake, J. R., "Non-spherical bubble dynamics in a compressible liquid. II. Acoustic standing wave," J. Fluid. Mech. **679**, 559–581 (2011).
Wang, Q. X. and Manmi, K., "Microbubble dynamics near a wall subjected to a travelling acoustic wave," Phys. Fluids **24**, 032104 (2014).
Wang, Q. X., Manmi, K., and Calvisi, M. L., "Numerical modeling of the 3D dynamics of ultrasound contrast agent microbubbles using the BIM," Phys. Fluids **27**, 022104 (2015).
Wang, Q. X., Yeo, K. S., Khoo, B. C., and Lam, K. Y., "Nonlinear interaction between gas bubble and free surface," Comput. Fluids **25**, 607–628 (1996).
Wang, Q. X., Yeo, K. S., Khoo, B. C., and Lam, K. Y., "Vortex ring modelling for toroidal bubbles," Theor. Comput. Fluid Dyn. **19**, 303–317 (2005).
Wu, G. X., "Hydrodynamic force on a rigid body during impact with liquid," J. Fluid. Struct. **12**, 549–559 (1998).
Young, F. R., *Cavitation* (McGraw-Hill, New York, 1989).
Zhang, S., Duncan, J. H., and Chahine, G. L., "The final stage of the collapse of a cavitation bubble near a rigid wall," J. Fluid. Mech. **257**, 147–181 (1993).
Zhang, S. and Duncan, J. H., "On the nonspherical collapse and rebound of a cavitation bubble," Phys. Fluids **6**, 2352–2362 (1994).
Zhang, A. M. and Liu, Y. L., "Improved three-dimensional bubble dynamics model based on boundary element method," J. Comput. Phys. **294**, 208–223 (2015).
Zhang, Y., Qian, Z., Ji, B., and Wu, Y., "A review of microscopic interactions between cavitation bubbles and particles in silt-laden flow," Renewable Sustainable Energy Rev. **56**, 303–318 (2016a).
Zhang, Y. L., Yeo, K. S., Khoo, B. C., and Chong, W. K., "Three dimensional computation of bubbles near a free surface," J. Comput. Phys. **146**, 105–123 (1998).
Zhang, Y. L., Yeo, K. S., Khoo, B. C., and Wang, C., "3D jet impact and toroidal bubbles," J. Comput. Phys. **16**, 336–360 (2001).
Zhang, S., Wang, S. P., and Zhang, A. M., "Experimental study on the interaction between bubble and free surface using a high-voltage spark generator," Phys. Fluids **28**, 032109 (2016b).